Trigonal Bipyramidal $M_2Ch_3^{2-}$ (M = Sn, Pb; Ch = S, Se, Te) and $TlMTe_3^{3-}$ Anions: Multinuclear Magnetic Resonance, Raman Spectroscopic, and Theoretical Studies, and the X-ray Crystal Structures of (2,2,2-crypt-K^+)$_3$$TlPbTe_3^{3-}$·2en and (2,2,2-crypt-$K^+$)$_2$$Pb_2Ch_3^{2-}$·0.5en (Ch = S, Se)†

Horst Borrmann,[1] Janette Campbell,[2] David A. Dixon,[3] Hélène P. A. Mercier,[2] Ayaaz M. Pirani,[2] and Gary J. Schrobilgen*,[2]

McMaster University, Hamilton, Ontario L8S 4M1, Canada, William R. Wiley Environmental Molecular Sciences Laboratory, Pacific Northwest National Laboratory, 906 Batelle Boulevard, P.O. Box 999, KI-83, Richland, Washington 99352, and Max Planck Institut für Festkörperforschung, Heisenbergstrasse 1, Stuttgart D-70569, Germany

Received May 20, 1998

The series of group 14 metal trigonal bipyramidal anions has been extended to the mixed group 13/group 14 metal $TlMTe_3^{3-}$ anions (M = Sn, Pb), obtained by the reaction of $Tl_2M_2Te_3$ and K_2Te in en or in en/ethylamine mixtures and a stoichiometric excess of 2,2,2-crypt with respect to K^+. The thallium anions were characterized in solution by ^{119}Sn, ^{205}Tl, ^{207}Pb, and ^{125}Te NMR spectroscopy. The small magnitudes of the relativistically corrected reduced coupling constants, $^1(K_{M-Ch})_{RC}$ and $^1(K_{Tl-Ch})_{RC}$, observed for the previously reported $M_2Ch_3^{2-}$ (Ch = Se, Te) and the $TlMTe_3^{3-}$ anions are consistent with predominantly p-bonded cages, and this observation is supported by local and nonlocal density functional theory (DFT) calculations. Theory indicates M−M and Tl−M interactions of high s character corresponding to Mayer bond orders of 0.13−0.32. The $(K_{M-M})_{RC}$ and $(K_{Tl-M})_{RC}$ couplings are unusually large compared to those of the butterfly-shaped $Tl_2Ch_2^{2-}$ anions and likely arise from higher M−M and Tl−M bond orders, a larger number of coupling pathways, and smaller M−Ch−M and M−Ch−Tl bond angles. The $TlPbTe_3^{3-}$ anion has also been structurally characterized by X-ray crystallography in (2,2,2-crypt-K^+)$_3$$TlPbTe_3^{3-}$·2en [monoclinic system, space group $P2_1/c$, $Z = 4$, $a = 15.256(5)$ Å, $b = 26.087(9)$ Å, $c = 20.984(8)$ Å, and $\beta = 93.03(3)°$] along with $Pb_2Ch_3^{2-}$ (Ch = S, Se) in (2,2,2-crypt-K^+)$_2$$Pb_2Ch_3^{2-}$·0.5en [$Pb_2S_3^{2-}$: triclinic system, space group $P\bar{1}$, $Z = 2$, $a = 10.189(2)$ Å, $b = 11.329(2)$ Å, $c = 23.194(4)$ Å, $\alpha = 95.439(14)°$, $\beta = 92.562(14)°$, and $\gamma = 90.549(14)°$; $Pb_2Se_3^{2-}$: triclinic system, space group $P\bar{1}$, $Z = 2$, $a = 10.187(2)$ Å, $b = 11.403(2)$ Å, $c = 23.360(6)$ Å, $\alpha = 95.26(2)°$, $\beta = 92.17(2)°$, and $\gamma = 90.89(2)°$]. Density functional theory calculations show that the experimental structures for the $M_2Ch_3^{2-}$ and $TlPbTe_3^{3-}$ anions are true minima and reproduce the experimental bond distances and angles. The vibrational frequencies determined by DFT calculations are in good agreement with those determined by Raman spectroscopy and have been used in their assignment.

Introduction

The trigonal bipyramidal $M_2Ch_3^{2-}$ (M = Sn, Pb; Ch = S, Se, and/or Te) and $SnPbSe_3^{2-}$ anions were previously synthesized and characterized by solution multi-NMR spectroscopy[4,5] and X-ray crystallography.[4−7] The structures of the $M_2Ch_3^{2-}$ (Ch = Se, Te) anions were determined by X-ray crystallography in the (2,2,2-crypt-K^+)$_2$$M_2Ch_3^{2-}$ salts and were shown to possess trigonal bipyramidal geometries in which three equatorial chalcogen atoms are bonded to the two axial group 14 metals and are compressed along the M−M axis. The small Ch−M−Ch (∼90°) and M−Ch−M (∼70°) bond angles and the small magnitudes of the relativistically corrected reduced coupling constants, $(K_{M-Ch})_{RC}$, suggested substantial valence p orbital involvement in the cage bonding and inert valence $5s^2$ and $6s^2$ electron lone pairs on M, consistent with a molecular bonding framework comprised of three valence p orbitals on M lying along the three M−Ch bonds and two valence p orbitals on each chalcogen atom, one lying along the M−Ch bond and the other, a nonbonding orbital, lying in the equatorial plane.[4,5] The $(K_{M-M})_{RC}$ couplings observed for the $Sn_2Se_3^{2-}$ and $SnPbSe_3^{2-}$ anions were significantly larger than the $(K_{M-Ch})_{RC}$ couplings, and the M−M distances observed in the X-ray crystal structures were significantly shorter than the sum of the van der Waals radii of M but significantly longer than the sum of the univalent radii of M. The large couplings were rationalized on the basis of multiple coupling pathways and through-space interactions of the valence s electrons on M, and the short M−M distances, on the basis of geometric constraints imposed by metal−chalcogen bonding.

The $M_2Ch_3^{2-}$ anions are structurally related to group 14 hetero[1.1.1]propellanes containing selenium in the equatorial positions. Short bridgehead−bridgehead distances have been

† Dedicated to the memory of Professor A. John Yarwood, October 13, 1938 − December 25, 1997.

(1) Max Planck Institut.
(2) McMaster University.
(3) Pacific Northwest National Laboratory.
(4) Björgvinsson, M.; Sawyer, J. F.; Schrobilgen, G. J. *Inorg. Chem.* **1987**, *26*, 741.
(5) Björgvinsson, M.; Mercier, H. P. A.; Mitchell, K. M.; Schrobilgen, G. J.; Strohe, G., *Inorg. Chem.* **1993**, *34*, 6046.
(6) Björgvinsson, M.; Sawyer, J. F.; Schrobilgen, G. J. *Inorg. Chem.* **1991**, *30*, 2231.
(7) Park, C.-W.; Salm, R. J.; Ibers, J. A. *Can. J. Chem.* **1995**, *73*, 1148.

10.1021/ic980574t CCC: $15.00
Published on Web 12/08/1998

Table 1. Summary of Crystal Data and Refinement Results for (2,2,2-crypt-K^+)$_3$$TlPbTe_3^{3-}$·2en, (2,2,2-crypt-$K^+$)$_2$$Pb_2S_3^{2-}$·0.5en, and (2,2,2-crypt-K^+)$_2$$Pb_2Se_3^{2-}$·0.5en

	(2,2,2-crypt-K^+)$_3$$TlPbTe_3^{3-}$·2en	(2,2,2-crypt-K^+)$_2$$Pb_2S_3^{2-}$·0.5en	(2,2,2-crypt-K^+)$_2$$Pb_2Se_3^{2-}$·0.5en
formula	$C_{58}H_{124}N_{10}O_{18}K_3TlPbTe_3$	$C_{38}H_{76}K_2N_4O_{12.5}Pb_2S_3$	$C_{38}H_{76}K_2N_4O_{12.5}Pb_2Se_3$
fw	2161.33	1377.79	1518.49
space group	$P2_1/c$ (No. 14)	$P\bar{1}$ (No. 2)	$P\bar{1}$ (No. 2)
a (Å)	15.256(5)	10.189(2)	10.187(2)
b (Å)	26.087(9)	11.329(2)	11.403(2)
c (Å)	20.984(8)	23.194(4)	23.360(6)
α (deg)	90	95.439(14)	95.26(2)
β (deg)	93.03(3)	92.562(14)	92.17(2)
γ (deg)	90	90.549(14)	90.89(2)
V (Å^3)	8339.6(51)	2662.5(8)	2699.9(10)
Z	4	2	2
T (°C)	24	−123	−183
ρ_{calcd} (g cm^{-3})	1.721	1.719	1.868
μ (cm^{-1})	28.15	66.5	84.6
R_1[a]	0.0437	0.0730	0.0479
wR_2[b]	0.0909	0.1975	0.1295

[a] $R_1 = \Sigma||F_o| - |F_c||/\Sigma|F_o|$ for $I > 2\sigma(I)$. [b] $wR_2 = [\Sigma[w(F_o^2 - F_c^2)^2]/\Sigma w(F_o^2)^2]^{1/2}$ for $I > 2\sigma(I)$.

observed in 2,4,5-triselena-1,3-disilabicyclo[1.1.1]pentane, i.e., $\{[(CH_3)_3Si)_3C]-Si\}_2Se_3$ (Si···Si, 2.515 Å)[8] and in the Ge analogue (Ge···Ge, 2.672 Å).[9] Unusually short transannular bridgehead−bridgehead distances have been calculated for the related oxygen analogues, the 2,4,5-trioxa-substituted bicyclo-[1.1.1]propellanes (Si, 2.089 Å; Ge, 2.260 Å; Sn, 2.475 Å).[10−12] Nagase[12] and Liang and Allen[13] have suggested that the bridgehead−bridgehead bonding interactions in hetero[1.1.1]-propellanes give rise to nonclassical structures in which these interactions are stabilized by means of three-center σ-bridged π bonds involving the bridgehead atom and one equatorial atom. In contrast, the calculated structures of the $M'H_2$-substituted group 14 bicyclo[1.1.1]propellanes, $M'_2(M'H_2)_3$ (M′ = Si, Ge, Sn),[10−12] indicate the absence of M′−M′ bonding interactions which was confirmed by a longer Sn−Sn distance [3.367(1) Å] observed in the X-ray crystal structure of 2,2,4,4,5,5-hexakis-(2,6-diethylphenyl)pentastanna[1.1.1]propellane.[14] The structural similarities between the hetero[1.1.1]propellanes and the $M_2Ch_3^{2-}$ anions suggest that the latter may also exhibit a degree of nonclassical bonding character. Short metal−metal distances have also been observed for mixed group 13 and 14 metal alkoxides, Sn(μ-OBu^t)$_3$M″ (M″ = In, Tl).[15,16]

The series of trigonal bipyramidal $M_2Ch_3^{2-}$ anions has now been extended to group 13. In the present work, the $TlSnTe_3^{3-}$ and $TlPbTe_3^{3-}$ anions have been characterized in solution by NMR spectroscopy and $TlPbTe_3^{3-}$ has been characterized by X-ray crystallography. The magnitudes of the relativistically corrected reduced Tl(I)−M(II) coupling constants and those determined from previous studies for Sn(II)−Sn(II) and Sn-(II)−Pb(II)[5] have been correlated with the results of density functional theory at the local (LDFT) and nonlocal (NLDFT) levels in order to gain insight into M−M coupling mechanisms and to establish whether they arise from significant M−M bonding interactions. The detailed structural characterization of the $Pb_2Ch_3^{2-}$ series is completed in the present study by the X-ray structure determination of the $Pb_2S_3^{2-}$ anion and the X-ray structure of the $Pb_2Se_3^{2-}$ anion has been reinvestigated at low temperature. The Raman spectra of the $M_2Ch_3^{2-}$ and $TlPbTe_3^{3-}$ anions have been recorded and assigned using the vibrational frequencies calculated from theory.

Results and Discussion

Synthesis of the $Pb_2Ch_3^{2-}$ (Ch = S, Se) and $TlMTe_3^{3-}$ (M = Sn, Pb) Anions. The experimental approach involved the syntheses of the ternary $KPb_{0.77}S$, $KPb_{0.5}Se$, and $Tl_2M_2Te_3$ (M = Sn, Pb) alloys by fusion of the elements followed by extraction of the powdered $KPb_{0.77}S$ and $KPb_{0.5}Se$ alloys in en in the presence of an excess of 2,2,2-crypt with respect to K^+ and by reaction of the powdered $Tl_2M_2Te_3$ alloys with K_2Te in en (Sn) or in a 1:1 v/v mixture of en/ethylamine (Pb) and in the presence of a molar excess of 2,2,2-crypt with respect to K^+. Single crystals of (2,2,2-crypt-K^+)$_2$$Pb_2Ch_3^{2-}$·0.5en (Ch = S, Se) were obtained by vapor-phase diffusion of THF into the en extracts. In a previous study, solvent evaporation led to the formation of unsolvated single crystals of (2,2,2-crypt-K^+)$_2$-$Pb_2Se_3^{2-}$.[4] Single crystals of (2,2,2-crypt-K^+)$_3$$TlPbTe_3^{3-}$·2en were obtained by vapor-phase diffusion of THF into an en/ethylamine solution previously studied by NMR spectroscopy.

X-ray Crystal Structures of (2,2,2-crypt-K^+)$_2$$Pb_2Ch_3^{2-}$·0.5en (Ch = S, Se) and (2,2,2-crypt-K^+)$_3$$TlPbTe_3^{3-}$·2en. A summary of the refinement results and crystal data are given in Table 1. The final atomic coordinates and equivalent isotropic thermal parameters for the heavy atoms are summarized in Table 2. The most significant bond distances and angles in the $Pb_2Ch_3^{2-}$ (Ch = S, Se) and $TlPbTe_3^{3-}$ anions are listed in Table 3.

The structures of the 2,2,2-crypt-K^+ cations in the three compounds are similar to those determined previously in K^+-(2,2,2-crypt-K^+)$_3$$Pb_9^{4-}$ [17] and K^+(2,2,2-crypt-K^+)$_2$$HOSnTe_3^{3-}$,[18] with average K−O [K−N] distances of 2.835(8) [2.978(19)] and 2.825(8) [3.040(21)] Å, respectively. A complete list of bond distances and angles in the 2,2,2-crypt-K^+ cations is given in the Supporting Information, Table S3.

The crystal structures of (2,2,2-crypt-K^+)$_2$$Pb_2Ch_3^{2-}$·0.5en consist of ordered assemblies of $Pb_2Ch_3^{2-}$ anions and 2,2,2-

(8) Yoshida, H.; Takahara, Y.; Erata, T.; Ando, W. *J. Am. Chem. Soc.* **1992**, *114*, 1098.
(9) Ando, W.; Watanabe, S.; Choi, N. *J. Chem. Soc., Chem. Commun.* **1995**, 1683.
(10) Nagase, S.; Kudo, T.; Kurakake, T. *J. Chem. Soc., Chem. Commun.* **1988**, 1063.
(11) Nagase, S.; Kudo, T. *Organometallics* **1988**, *7*, 2534.
(12) Nagase, S. *Polyhedron* **1991**, *10*, 1299.
(13) Liang, C.; Allen, L. C. *J. Am. Chem. Soc.* **1991**, *113*, 1878.
(14) Sita, L. R.; Bickerstaff, R. D. *J. Am. Chem. Soc.* **1989**, *111*, 6454.
(15) Veith, M.; Rösler, R. *Angew. Chem., Int. Ed. Engl.* **1982**, *21*, 858.
(16) Veith, M.; Kunze, K.; *Angew. Chem., Intl. Ed. Engl.* **1991**, *30*, 95.
(17) Campbell, J.; Dixon, D. A.; Mercier, H. P. A.; Schrobilgen, G. J. *Inorg. Chem.* **1995**, *34*, 5798.
(18) Campbell, J.; Devereux, L. A.; Gerken, M.; Mercier, H. P. A.; Pirani, A. M.; Schrobilgen, G. J. *Inorg. Chem.* **1996**, *35*, 2945.

Table 2. Atomic Coordinates ($\times 10^4$) and Equivalent Isotropic Thermal Parameters (Å^2 $\times$ 10^3) for (2,2,2-crypt-K$^+$)$_2$Pb$_2$S$_3^{2-}$·0.5en, (2,2,2-crypt-K$^+$)$_2$Pb$_2$Se$_3^{2-}$·0.5en, and (2,2,2-crypt-K$^+$)$_3$TlPbTe$_3^{3-}$·2en

	x	*y*	*z*	*U*(eq)[a]
(2,2,2-crypt-K$^+$)$_2$Pb$_2$S$_3^{2-}$·0.5en				
Pb(1)	6510(1)	8171(1)	7830(1)	44(1)
Pb(2)	9466(1)	8097(1)	7490(1)	34(1)
S(1)	7703(2)	6386(2)	7243(1)	31(1)
S(2)	7707(2)	9672(2)	7212(1)	35(1)
S(3)	8604(4)	8402(3)	8540(1)	57(1)
(2,2,2-crypt-K$^+$)$_2$Pb$_2$Se$_3^{2-}$·0.5en				
Pb(1)	498(1)	6875(1)	2509(1)	14(1)
Pb(2)	3509(1)	6841(1)	2128(1)	19(1)
Se(1)	2301(1)	8695(1)	2747(1)	13(1)
Se(2)	2346(1)	5258(1)	2791(1)	15(1)
Se(3)	1336(1)	6546(1)	1403(1)	27(1)
(2,2,2-crypt-K$^+$)$_3$TlPbTe$_3^{3-}$·2en				
Pb(1)	4393(1)	−679(1)	−1863(1)	80(1)
Tl(1)	4393(1)	−679(1)	−1863(1)	80(1)
Te(1)	5000	293(1)	−2500	89(1)
Te(2)	6219(1)	−1171(1)	−1856(1)	70(1)

[a] *U*(eq) is defined as one-third of the trace of the orthogonalized $\mathbf{U}_{ij}$ tensor.

crypt-K$^+$ cations and positionally disordered en solvent molecules, whereas the crystal structure of (2,2,2-crypt-K$^+$)$_3$TlPbTe$_3^{3-}$·2en consists of a positionally disordered anion and ordered cations and solvent molecules. The title compounds contain trigonal bipyramidal anions of approximate D_{3h} (Pb$_2$Ch$_3^{2-}$) and C_{3v} (TlPbTe$_3^{3-}$) point symmetries (Figure 1) which are isostructural with the previously characterized M$_2$Ch$_3^{2-}$ (M = Sn, Pb; Ch = Se, Te) anions. The anions in the title compounds, as well in the previously characterized structures,[4-7] possess short apical metal−metal distances, which are a general feature among structures containing trigonal bipyramidal X$_2$Y$_3$ units [(*t*-Bu)$_2$Si$_2$P$_3$(C$_6$H$_{11}$)$_3$, Si−Si = 2.518(3) Å;[19] ((Me$_3$Si)$_3$C)$_2$M$_2$Se$_3$, M−M = 2.515 (Si),[8] 2.672 (Ge) Å;[9] Pn$_2$(W(CO)$_5$)$_3$, Pn−Pn = 2.279(4) (As),[20] 2.663(3) (Sb),[21] 2.818(3) (Bi)[22] Å] and XX′Y$_3$ units [SnMO$_3$(*t*-Bu)$_3$,[15] Sn−M = 3.200(3) (In), 3.306-(3) (Tl) Å; (CO)$_5$MoSnTlO$_3$(*t*-Bu)$_3$,[16] Sn−Tl = 3.298(1) Å; ((CO)$_5$Mo)$_2$SnInO$_3$(*t*-Bu)$_3$,[16] Sn−In = 3.078(1) Å]. The apical Pb−Pb distance in Pb$_2$S$_3^{2-}$ [3.1467(7) Å] is shorter than those observed in Pb$_2$Se$_3^{2-}$ [3.2260(8) Å] and Pb$_2$Te$_3^{2-}$ [3.249(2) and 3.232(1) Å]. The Pb−Pb distances of all three chalcogens are significantly longer than the reported single-bond Pb−Pb distances of 2.844(4) Å in Ph$_6$Pb$_2$[23] and 2.908(1) Å in Ph$_3$Pb·Pb[C(SiMe$_3$)$_3$]Ph$_2$[24] but are comparable to the intermetallic distances reported for the M$_9$ clusters [e.g., Pb$_9^{3-}$, 3.050(3)−3.627(3) Å; Pb$_9^{4-}$, 3.0639(14)−3.4510(13) Å].[17] The Tl−Pb distance in TlPbTe$_3^{3-}$ [3.332(2) Å] is significantly longer than the Pb−Pb distance observed in Pb$_2$Te$_3^{2-}$.[6,7] The M−M distances parallel the covalent radii of the chalcogens, increasing in the order S < Se < Te in the tin and lead anion series.

The Pb−S distances [2.618(3)−2.664(2) Å] are very similar to those observed in the trigonal pyramidal Pb(SPh)$_3^-$ anion [2.619(1)−2.647(1) Å][25] but are shorter than those found in (Ph$_3$P)$_4$Pt$_2$S$_2$Pb(NO$_3$)$_2$ [2.692(4) and 2.774(4) Å][26] and in (Ph$_3$P)$_4$Pt$_2$S$_2$Pb(NO$_3$)(PF$_6$) [2.766(3) Å],[26] with the exception of the shorter Pb−S distance [2.641(3) Å] reported for the PF$_6^-$ salt. Similarly, the Pb−Se distances [2.7340(10)−2.7796(10) Å] are nearly identical to those observed in Pb(SePh)$_3^-$ [2.727-(1)−2.762(1) Å].[25] The M−Te distances [3.0324(14)−3.067-(13) Å] in TlPbTe$_3^{3-}$ are averages of the Pb(II)−Te and Tl(I)−Te distances owing to the symmetry equivalence of the Tl and Pb atoms. Comparable Pb(II)−Te and Tl(I)−Te distances have been observed in the Pb$_2$Te$_3^{2-}$ [2.943(1)[6] and 2.971(2) Å[7]] and in the butterfly-shaped Tl$_2$Te$_2^{2-}$ [2.956(2)[27] and 2.954(11) Å[28]] anions.

The Ch−Pb−Ch bond angles observed in the Pb(ChPh)$_3^-$ anions [S, 90.32(4)−96.14(5)°; Se, 88.82(4)−96.57(4)°][25] are slightly larger than those in Pb$_2$Ch$_3^{2-}$. The angle trends among the Pb$_2$Ch$_3^{2-}$ anions, i.e., S−Pb−S < Se−Pb−Se < Te−Pb−Te and Pb−S−Pb > Pb−Se−Pb > Pb−Te−Pb, are in accord with the VSEPR rules,[29] i.e., the Ch−Pb−Ch bond angles decrease while the Pb−Ch−Pb bond angles increase with increasing electronegativity of the chalcogen, and are reproduced theoretically (see "Computational Results").

The equatorial Ch···Ch distances (S, 3.605−3.731 Å; Se, 3.796−3.932 Å; Te, 4.427 Å) are comparable to the sum of the respective van der Waals radii (S, 3.7 Å; Se, 4.0 Å; Te, 4.4 Å)[30] and are in accord with localized valence structures involving two-center two-electron M−Ch bonds.

The anisotropies of all the atoms of the Pb$_2$Se$_3^{2-}$ anion at −183 °C are smaller than those observed at 24 °C[4] with the anisotropy of Se(3) exhibiting the greatest difference in the *x* direction, i.e., perpendicular to the equatorial plane [U_{eq} = 0.048(4) Å^2, −183 °C, and U_{eq} = 0.150(8) Å^2, 24 °C].[4] However, and as previously observed at 24 °C, the apical atoms and one equatorial chalcogen atom, Se(3), still exhibit elongated thermal ellipsoids with the two apical atoms directed toward the more anisotropic Se(3) atom. This can be explained in terms of a rocking motion about the Se(1)−Se(2) axis which appears to be a consequence of packing effects and is consistent with the similar environments observed for the Se(1) and Se(2) atoms. In addition, shorter anion···cation contacts are observed for Se-(1) and Se(2) than for Se(3). The Se(1)···CH$_2$ [3.747 Å] and Se(2)···CH$_2$ [3.688 Å] distances are smaller than the sum of their van der Waals radii [Se···CH$_2$ = 4.0 Å][30] whereas the shortest Se(3)···CH$_2$ distance [3.921 Å] is at the sum of their van der Waals radii. Similar behavior has been noted in the low-temperature structures of Pb$_2$S$_3^{2-}$ (−123 °C; this work) and in Pb$_2$Te$_3^{2-}$ (−160 °C)[7] showing that the origin of the anisotropy in these closely related structures does not arise from a disorder but from an anion rocking motion.

Multi-NMR Spectra of the TlMTe$_3^{3-}$ (M = Sn, Pb) Anions. The TlMTe$_3^{3-}$ anions were identified in solution by natural abundance ^{119}Sn, ^{205}Tl, ^{207}Pb, and ^{125}Te NMR spectroscopy.[31] The experimental and simulated ^{119}Sn, ^{205}Tl, ^{207}Pb, and ^{125}Te NMR spectra are depicted in Figures 2 and 3. The

(19) Dreiss, M.; Gleiter, R.; Janoschek, R.; Pritzkow, H.; Reisgys, M. *Angew. Chem., Int. Ed. Engl.* **1994**, *33*, 1484.
(20) Sigwarth, B.; Zsolnai, L.; Berke, H.; Huttner, G. *J. Organomet. Chem.* **1982**, *226*, C5.
(21) Huttner, G.; Weber, U.; Sigwarth, B.; Scheidsteger, O. *Angew. Chem., Int. Ed. Engl.* **1982**, *21*, 411.
(22) Huttner, G.; Weber, U.; Zsolnai, L. *Z. Naturforsch.* **1982**, *B37*, 707.
(23) Preut, H.; Haupt, H. J.; Huber, F. *Z. Anorg. Allg. Chem.* **1972**, *388*, 165.
(24) Mallela, S. P.; Myrczek, J.; Bernal, I.; Geanangel, R. A. *J. Chem. Soc., Dalton Trans.* **1993**, 2891.
(25) Dean, P. A. W.; Vittal, J. J.; Payne, N. C. *Inorg. Chem.* **1984**, *23*, 4232.
(26) Zhou, M.; Xu, Y.; Lam, C.-F.; Koh, L.-L.; Mok, K. F.; Leung, P.-H.; Hor, T. S. A. *Inorg. Chem.* **1993**, *32*, 4660.
(27) Borrmann, H.; Campbell, J.; Dixon, D. A.; Mercier, H. P. A.; Pirani, A. M.; Schrobilgen, G. J. *Inorg. Chem.*, **1998**, *37*, 1929.
(28) Burns, R. C.; Corbett, J. D. *J. Am. Chem. Soc.* **1981**, *103*, 2627.
(29) Gillespie, R. J.; Hargittai, I. *The VSEPR Model of Molecular Geometry*; Simon & Schuster, Inc.: Boston, MA, 1991; Chapters 3 and 5.
(30) Pauling, L. *The Nature of the Chemical Bond*, 3rd ed.; Cornell University Press: Ithaca, NY, 1960; pp 260, 261.
(31) Mason, J. In *Multinuclear NMR*; Mason, J., Ed.; Plenum Press: New York, 1987; Appendix, pp 627, 629.

Table 3. Experimental and Calculated Geometric Parameters for the $M_2Ch_3^{2-}$, $TlMTe_3^{3-}$ (M = Sn, Pb; Ch = S, Se, Te), and $SnPbSe_3^{2-}$ Anions

	$Sn_2S_3^{2-}$			$Sn_2Se_3^{2-}$				$Sn_2Te_3^{2-}$			
	DZVP/DZVP		ECP/DZP		DZVP/DZVP		ECP/ECP		DZVP/DZVP		ECP/ECP
	LDFT	NLDFT	LDFT	expt[a,b]	LDFT	NLDFT	LDFT	expt[a,b]	LDFT	NLDFT	LDFT
M−M (Å)	3.099	3.146	3.084	3.090(3)	3.167	3.221	3.167	3.270(6)	3.270	3.323	3.255
M−Ch (Å)	2.574	2.622	2.584	2.654(5)	2.703	2.762	2.748	2.887(4)	2.926	2.989	2.987
Ch···Ch (Å)	3.56	3.64	3.59	3.471	3.79	3.89	3.89	4.103	4.20	4.30	4.34
<MChM (deg)	74.1	73.7	73.3	71.1(1)	71.7	71.4	70.4	68.7(1)	68.0	67.3	66.0
<ChMCh (deg)	87.5	87.7	88.0	89.6(2)	89.2	89.4	90.1	90.9(2)	91.8	92.8	93.1

	$Pb_2S_3^{2-}$					$Pb_2Se_3^{2-}$					$Pb_2Te_3^{2-}$					
		PP/DZVP2		PP/PP	ECP/DZP		PP/DZVP		PP/PP	ECP/ECP			PP/DZVP		PP/PP	ECP/ECP
	expt[a,c]	LDFT	NLDFT	LDFT	LDFT	expt[a,c]	LDFT	NLDFT	LDFT	LDFT	expt[a,d,[e]]		LDFT	NLDFT	LDFT	LDFT
M−M (Å)	3.1467(7)	3.004	3.008	3.023	3.110	3.2260(8)	3.061	3.073	3.020	3.156	3.249(2)	[3.232(1)]	3.105	3.113	3.041	3.207
M−Ch (Å)	2.640(5)	2.660	2.685	2.633	2.616	2.757(11)	2.792	2.820	2.719	2.775	2.943(2)	[2.971(4)]	2.980	3.015	2.921	3.003
Ch···Ch (Å)	3.671(6)	3.78	3.85	3.71	3.64	3.872(4)	3.99	4.03	3.93	3.95	4.25	[4.318]	4.41	4.47	4.32	4.40
<MChM (deg)	73.2(4)	68.4	68.2	70.1	72.9	70.7(7)	66.6	66.2	67.5	69.3	67.01(6)	[65.89(5)]	62.8	62.2	62.7	64.5
<ChMCh (deg)	88.1(5)	91.6	91.7	90.3	88.3	89.2(4)	92.8	93.0	92.1	90.9	92.46(4)	[93.23(6)]	95.4	95.8	95.4	94.1

	$TlPbTe_3^{3-}$				$SnPbSe_3^{2-}$				$TlSnTe_3^{3-}$	
		PP/PP/DZVP2	ECP/ECP/ECP	PP/PP/DZVP2		PP/DZVP/DZVP		ECP/ECP/ECP		ECP/ECP/ECP
	expt[a,c]	LDFT	LDFT	NLDFT		LDFT	NLDFT	LDFT		LDFT
Tl−Pb (Å)	3.332(2)	3.141	3.173	3.162	Sn−Pb (Å)	3.130	3.162	3.158	Sn−Tl (Å)	3.281
Pb−Te (Å)		2.937	3.030	2.964	Sn−Se (Å)	2.727	2.781	2.752	Tl−Te (Å)	3.240
Tl/Pb−Te	3.0670(1) × 2; 3.032(1)	3.060[f]	3.132[f]	3.099[f]	Pb−Se (Å)	2.771	2.800	2.769	Sn−Te (Å)	3.013
Tl−Te (Å)		3.183	3.234	3.234	Se···Se (Å)	3.91	3.98	3.92	Te···Te (Å)	4.60
Te···Te (Å)	4.427 × 2; 4.479	4.53	4.61	4.60	Sn−Se−Pb (deg)	69.4	69.0	69.8	Sn−Te−Tl (deg)	63.2
Tl−Te−Pb (deg)	66.65(4) × 2; 65.66(3)	61.6	60.8	61.2	Se−Sn−Se (deg)	91.7	91.5	90.9	Te−Sn−Te (deg)	99.5
Te−Pb−Te (deg)		101.7	100.7	101.8	Se−Pb−Se (deg)	89.8	90.7	90.2	Te−Tl−Te (deg)	90.4
Te−Tl/Pb−Te (deg)	93.33(4) × 2; 92.84(3)	96.3[g]	96.6[g]	96.3[g]						
Te−Tl−Te (deg)		90.8	92.4	90.7						

[a] Average values. [b] Reference 5. [c] Present work. [d] Reference 6. [e] Reference 7. [f] Average value of calculated Pb−Te and Tl−Te. [g] Average value of calculated ∠Te−Pb−Te and ∠Te−Tl−Te.

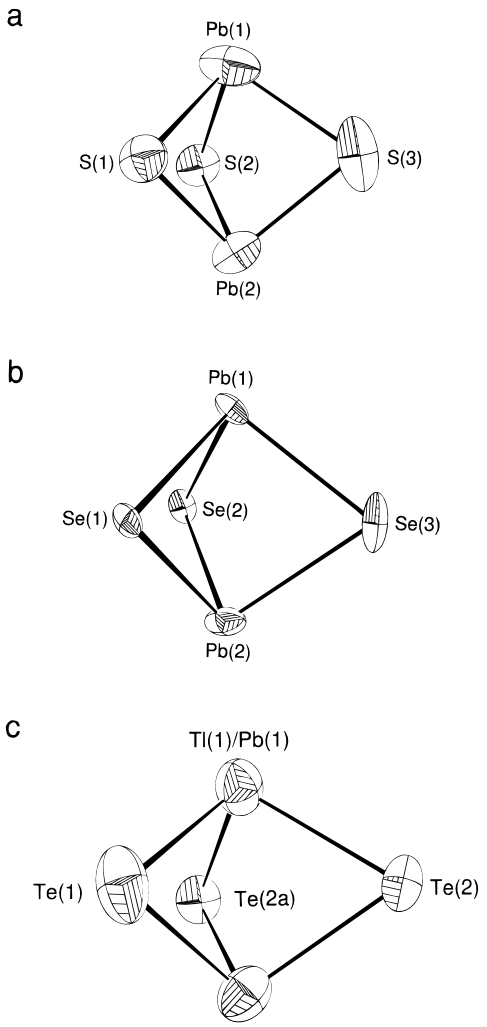

Figure 1. Views of the (a) $Pb_2S_3^{2-}$, (b) $Pb_2Se_3^{2-}$, and (c) $TlPbTe_3^{3-}$ anions in (2,2,2-crypt-K^+)$_2Pb_2Ch_3^{2-}$·0.5en (Ch = S, Se) and (2,2,2-crypt-K^+)$_3TlPbTe_3^{3-}$·2en with displacement ellipsoids drawn at the 75% (a) and (b) and 50% (c) probability levels.

chemicalshifts and spin−spin coupling constants of the $TlMTe_3^{3-}$ anions as well as those of the previously characterized $M_2Ch_3^{2-}$, $SnPbSe_3^{2-}$, and $Tl_2Ch_2^{2-}$ anions are listed in Table 4. The number of observed environments, the doublet and satellite doublet spacings corresponding to $J(^{207}Pb-^{203,205}Tl)$, $J(^{119}Sn-^{203,205}Tl)$, $J(^{207}Pb-^{123,125}Te)$, $J(^{205}Tl-^{123,125}Te)$, and $J(^{119}Sn-^{123,125}Te)$, and the satellite to central peak intensity ratios are consistent with trigonal bipyramidal $TlMTe_3^{3-}$ structures having C_{3v} point symmetries and are supported by the trigonal bipyramidal geometry observed for the $TlPbTe_3^{3-}$ anion in the solid state.

$TlSnTe_3^{3-}$. The NMR spectra of the deep red solution obtained by reacting $Tl_2Sn_2Te_3$ and K_2Te in a 1.0:1.4 molar ratio in en were recorded at 0 °C and gave rise to a new resonance in the ^{119}Sn, ^{205}Tl, and ^{125}Te spectra as well as to several weak signals which were assigned to the previously characterized $SnTe_3^{2-}$ [32] [$\delta(^{119}Sn) = -1160$ ppm, $\delta(^{125}Te) = -410$ ppm, $^1J(^{119}Sn-^{125}Te) = 4549$ Hz], HTe^- [33] [$\delta(^{125}Te) = -1094$ ppm, $^1J(^{125}Te-^1H) = 122$ Hz], and $Tl_2Te_2^{2-}$ [27] [$\delta(^{205}Tl) = 8182$ ppm, $^1J(^{205}Tl-^{125}Te) = 6348$ Hz] anions. The new ^{119}Sn, ^{205}Tl, and ^{125}Te resonances (Figure 2) belong to the $TlSnTe_3^{3-}$ anion. They are assigned in Table 4 and discussed below.

The ^{119}Sn NMR spectrum of the $TlSnTe_3^{3-}$ anion was observed in the Sn(II) region and consisted of an intense, sharp doublet arising from coupling to one thallium atom. The doublet was split into its $J(^{119}Sn-^{205}Tl) = 6533$ Hz and $J(^{119}Sn-^{203}Tl) = 6474$ Hz components with the ratio, $J(^{119}Sn-^{205}Tl)/J(^{119}Sn-^{203}Tl) = 1.009$, in excellent agreement with the ratio of the gyromagnetic ratios $\gamma(^{205}Tl)/\gamma(^{203}Tl) = 1.010$.[31] The doublet was accompanied by a pair of satellites arising from $^1J(^{119}Sn-^{123,125}Te)$. The intensities of the $^{123,125}Te$ satellites relative to the central doublet indicated that the tin environment was coupled to three chemically equivalent tellurium atoms (see spectral simulation, Figure 2, and Table 5). The ^{205}Tl NMR resonance of $TlSnTe_3^{3-}$ was observed in the Tl(I) region and consisted of a singlet flanked by three sets of symmetric doublet satellites arising from $J(^{205}Tl-^{125}Te) = 221$ Hz, $J(^{205}Tl-^{119}Sn) = 6533$ Hz, and $J(^{205}Tl-^{117}Sn) = 6251$ Hz [(6533 Hz)/(6251 Hz) = 1.046, $\gamma(^{119}Sn)/\gamma(^{117}Sn) = 1.046$].[31] In addition, four weaker satellites were observed in the ^{205}Tl NMR spectrum of $TlSnTe_3^{3-}$ (Figure 2) and also arise from $J(^{205}Tl-^{125}Te)$. The ^{125}Te NMR signal of the anion centered at −887 ppm comprised a doublet arising from $^1J(^{125}Te-^{203,205}Tl)$ coupling and accompanying unresolved $^{117,119}Sn$ satellites corresponding to $^1J(^{125}Te-^{117,119}Sn) = 1190$ Hz.

$TlPbTe_3^{3-}$. The ^{205}Tl, ^{207}Pb, and ^{125}Te NMR spectra of a deep red solution obtained by reacting $Tl_2Pb_2Te_3$ and K_2Te in a 1.0:1.6 molar ratio in en/ethylamine (1:1 v/v) in the presence of a molar excess of 2,2,2-crypt with respect to K^+ were recorded at 0 °C. The signal at −1094 ppm in the ^{125}Te NMR spectrum was assigned to HTe^-. All remaining resonances in the ^{125}Te, ^{205}Tl, and ^{207}Pb NMR spectra arose from the $TlPbTe_3^{3-}$ anion (Figure 3). In addition to $TlPbTe_3^{3-}$, the known $TlTe_3^{3-}$ [32] and $Pb_2Te_3^{2-}$ [4] anions were also detected at 24 °C in a red-brown solution obtained by reacting $Tl_2Pb_2Te_3$ and K_2Te (1.0:1.4 molar ratio) in en in the presence of a 50 mol % excess of 2,2,2-crypt. However, the resonances corresponding to the $TlPbTe_3^{3-}$ anion at 24 °C were broad and precluded measurement of relative satellite intensities. Consequently, subsequent discussion of the NMR parameters for the $TlPbTe_3^{3-}$ anion refers to spectra obtained at 0 °C in the mixed solvent en/ethylamine (6.7 mol % ethylamine).

The ^{205}Tl, ^{207}Pb, and ^{125}Te NMR spectra of $TlPbTe_3^{3-}$ were similar to those observed for the $TlSnTe_3^{3-}$ anion (Figure 3). The ^{207}Pb NMR resonance (2188 ppm) consisted of a doublet split into $J(^{207}Pb-^{205}Tl) = 13\,086$ Hz and $J(^{207}Pb-^{203}Tl) = 12\,962$ Hz components [(13 086 Hz)/(12 962 Hz) = 1.010, $\gamma(^{205}Tl)/\gamma(^{203}Tl) = 1.010$] and accompanying unresolved $^{123,125}Te$ satellites [$^1J(^{207}Pb-^{123,125}Te) = 280$ Hz]. The intensities of the $^{123,125}Te$ satellites indicated that the lead environment was coupled to three chemically equivalent tellurium atoms (see spectral simulation, Figure 3, and Table 5). The ^{205}Tl NMR spectrum of $TlPbTe_3^{3-}$ comprised a singlet (3483 ppm) symmetrically flanked by satellite doublets arising from, $^1J(^{205}Tl-^{123,125}Te) = 307$ Hz and $J(^{205}Tl-^{207}Pb) = 13\,086$ Hz. A broad doublet at −944 ppm in the ^{125}Te NMR spectrum of $TlPbTe_3^{3-}$ was assigned to $^1J(^{125}Te-^{203,205}Tl)$, and the associated satellite doublet to $^1J(^{125}Te-^{207}Pb)$.

The ^{119}Sn, ^{205}Tl, ^{207}Pb, and ^{125}Te NMR spectra of the $TlMTe_3^{3-}$ (M = Sn, Pb) anions were simulated by using the natural abundances of the spin-$^1/_2$ nuclei ^{117}Sn, ^{119}Sn, ^{203}Tl, ^{205}Tl, ^{207}Pb, and ^{125}Te;[31] the values of the observed coupling constants (Table 4); and the most abundant (≥1.4 mol %) isotopomers (Table 5) contributing significant first-order sub-

(32) Burns, R. C.; Devereux, L. A.; Granger, P.; Schrobilgen, G. J. *Inorg. Chem.* **1985**, *24*, 2615.
(33) Björgvinsson, M.; Schrobilgen, G. J. *Inorg. Chem.* **1991**, *30*, 2540.

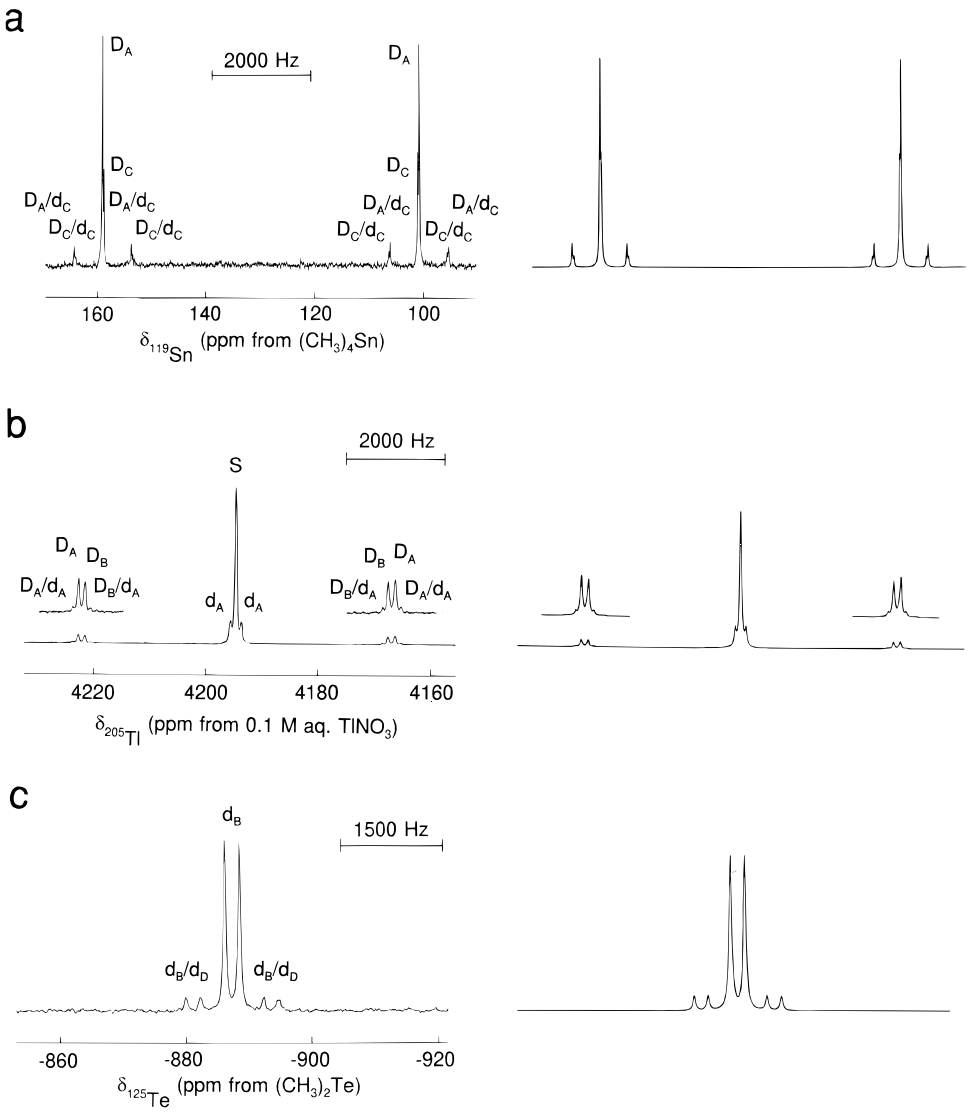

Figure 2. Observed (left trace) and simulated (right trace) (a) ^{119}Sn (111.922 MHz), (b) ^{205}Tl (115.444 MHz), and (c) ^{125}Te (94.692 MHz) of $TlSnTe_3^{3-}$ at 0 °C. The symbols used to label the peaks are defined in Table 5.

spectra to the experimental ^{119}Sn, ^{205}Tl, ^{207}Pb, and ^{125}Te NMR spectra. The resulting simulations (Figures 2 and 3) are in excellent agreement with the experimental spectra, accounting for all the observed satellite peaks and their relative intensities. The spin−spin coupling constants listed in Table 4 are assigned in Figures 2 and 3 and in Table 5.

Vibrational Spectra of the $M_2Ch_3^{2-}$ (M = Sn, Pb; Ch = S, Se, Te) and $TlPbTe_3^{3-}$ Anions. The solid-state Raman spectra of (2,2,2-crypt-K^+)$_2Pb_2S_3^{2-}$·0.5en, (2,2,2-crypt-K^+)$_2M_2Se_3^{2-}$, (2,2,2-crypt-K^+)$_2M_2Te_3^{2-}$, and (2,2,2-crypt-K^+)$_3TlPbTe_3^{3-}$·2en are shown in Figure 4 and cover only those spectral regions in which the fundamental vibrations of the anions are found. The observed and calculated frequencies and their assignments are listed in Table 6, and a description of the free anion vibrational modes is provided in Figure 5.[34] Calculated frequencies for $SnPbSe_3^{2-}$ and $TlSnTe_3^{3-}$ are also reported. Anion assignments were assisted by LDFT and NLDFT calculations, and, as expected, the vibrational frequencies at the nonlocal level are lower in energy than at the local level.[27]

The vibrational modes of the gas-phase $M_2Ch_3^{2-}$ anions belong to the reducible representation $2A_1' + 2E' + A_2'' + E''$ under D_{3h} point symmetry. A total of six vibrational bands (nine modes) are expected, of which five bands ($2A_1' + 2E' + E''$) are Raman active and three bands ($A_2'' + 2E'$) are infrared active. In $M_2S_3^{2-}$, $Sn_2Te_3^{2-}$, and $Pb_2Se_3^{2-}$, the highest frequency A_1' mode is the antisymmetric combination of the M and Ch motions toward and away from the center of mass, respectively. The next highest frequency A_1' mode can be described as the in-plane symmetric motions of the Ch and M atoms away from the center of mass. As expected, the calculated frequencies of the symmetric stretch show a significant decrease upon increasing the mass of the chalcogen but the difference is not as large when M = Sn or Pb. The $Sn_2Se_3^{2-}$ and $Pb_2Te_3^{2-}$ anions have the order of their two A_1' modes reversed and is presumably a consequence of the smaller difference in mass between M and Ch. The A_2'' mode is the out of plane motion of the Ch atoms coupled to the asymmetric motion of the two M atoms toward and away from the Ch_3 plane. The highest energy E′ mode occurs at slightly higher energy than the A_2'' mode and corresponds to an asymmetric stretch in which an equatorial Ch moves in a direction opposite to the axial M atoms and the other Ch atoms are moving toward the center of mass. This mode is predicted to be the most intense band in the infrared spectrum and the absolute infrared intensity of the E′ stretch is

(34) Mukherjee, A.; Spiro, T. G. SVIB program 656, Bulletin 15(1); Quantum Chemistry Program Exchange, Indiana University, 1995.

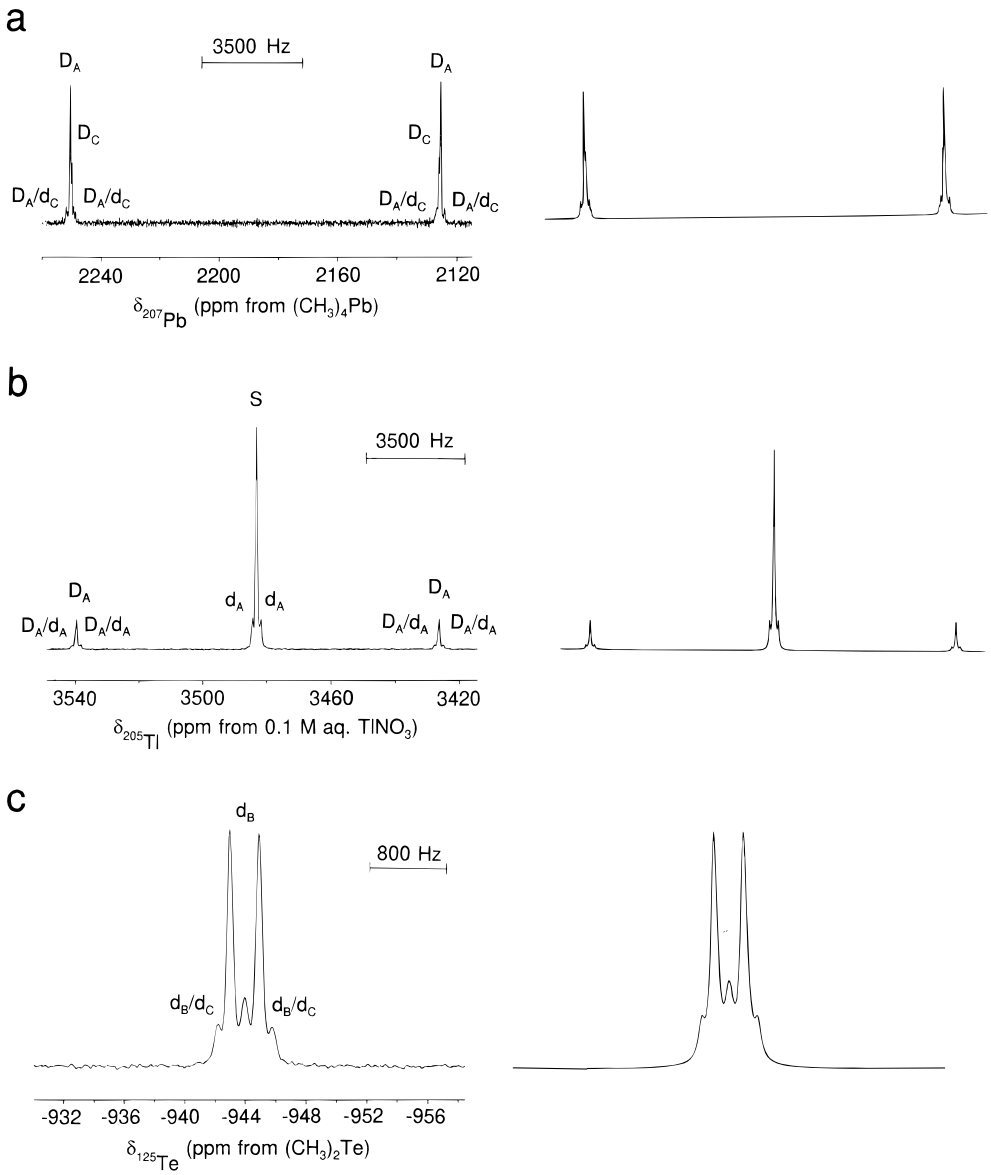

Figure 3. Observed (left trace) and simulated (right trace) (a) ^{207}Pb (104.631 MHz), (b) ^{205}Tl (115.444 MHz), and (c) ^{125}Te (157.794 MHz) of $TlPbTe_3^{3-}$ at −20 °C. The symbols used to label the peaks are defined in Table 5.

predicted to decrease with increasing size of Ch. The lowest frequency mode is the E′ in-plane bend in which two Ch atoms move toward each other and away from the third Ch atom in the Ch_3 plane with the axial M atoms translating parallel and in the same direction as the unique Ch atom. This mode is expected to be weak in the infrared spectrum. The E″ mode is the out-of-plane bend and is expected to be higher in energy than the E′ bend. The mode is described as the out of Ch_3-plane motion of two Ch atoms in opposite directions to each other in their respective [M,Ch,M] planes with the M atoms moving in opposite directions to each other and perpendicular to the [M,Ch,M] plane containing the undisplaced Ch atom.

The gas-phase $TlPbTe_3^{3-}$ anion possesses C_{3v} point symmetry and its vibrational modes belong to the irreducible representation $3A_1 + 3E$ where the A_1 modes and E modes are both Raman and infrared active. Because the lead and thallium atoms have similar masses, the descriptions of their modes under C_{3v} symmetry are very similar to those for the $Pb_2Ch_3^{2-}$ anions under D_{3h} symmetry and are correlated as follows ($D_{3h} \rightarrow C_{3v}$): $\nu_1(A_1') \rightarrow \nu_1(A_1)$; $\nu_2(A_1') \rightarrow \nu_2(A_1)$ for $TlPbTe_3^{3-}$ and $\nu_2(A_1') \rightarrow \nu_3(A_1)$ for $TlSnTe_3^{3-}$ and $SnPbSe_3^{2-}$; $\nu_3(E') \rightarrow \nu_4(E)$; $\nu_4(E') \rightarrow \nu_6(E)$; $\nu_5(A_2'') \rightarrow \nu_3(A_1)$ for $TlPbTe_3^{3-}$ and $\nu_5(A_2'') \rightarrow \nu_2(A_1)$ for $TlSnTe_3^{3-}$ and $SnPbSe_3^{2-}$; and $\nu_6(E'') \rightarrow \nu_5(E)$.

Vibrational activities of the $M_2Ch_3^{2-}$ and $TlPbTe_3^{3-}$ anions in their respective unit cells have been determined by correlation of the gas-phase $M_2Ch_3^{2-}$ (D_{3h}) and $TlPbTe_3^{3-}$ (C_{3v}) anion symmetries to the crystallographic anion site and unit cell symmetries (Table S14).[35] The $Pb_2S_3^{2-}$ anion, when correlated with the anion site symmetry C_1 and the unit cell symmetry C_i (space group $P\bar{1}$) is predicted to have six Raman active bands having A_g symmetry and six infrared active bands having A_u symmetry. Each of the bands of the $M_2Se_3^{2-}$ anions, when correlated to the anion site symmetry (C_1) and the unit cell symmetry, C_{2h} (space group $P2_1/n$), should be split into A_g and B_g components in the Raman spectrum and A_u and B_u components in the infrared spectrum so that all vibrational modes are active but split in both the Raman and infrared spectra. The unit cells in which the $M_2Te_3^{2-}$ anions occur both possess D_{3d} symmetry (space group $P\bar{3}c_1$)

(35) Carter, R. J. *J. Chem. Educ.* **1971**, *48*, 297 and references therein.

Table 4. Chemical Shifts and Spin−Spin Coupling Constants for the $TlMTe_3^{3-}$,[a] $M_2Ch_3^{2-}$,[b,c] $SnPbSe_3^{2-}$,[c] and $Tl_2Ch_2^{2-}$ [d] Anions (M = Sn, Pb; Ch = Se, Te)

			chemical shift, ppm				coupling constant, Hz			reduced coupling const, $T^2\,J^{-1} \times 10^{20}$			
anion	solvent	T (°C)	^{119}Sn	^{205}Tl	^{207}Pb	Ch	J(M−Ch) or $J(^{205}\text{Tl}-\text{Ch})$	J(M−M) or $J(^{205}\text{Tl}-\text{M})$	% s M−Ch	K_{M-Ch} or K_{Tl-Ch}	$(K_{M-Ch})_{RC}$ or $(K_{Tl-Ch})_{RC}$	K_{M-M} or K_{Tl-M}	$(K_{M-M})_{RC}$ or $(K_{Tl-M})_{RC}$
$TlSnTe_3^{3-}$	en	0	130	4196		−887	1180 (^{119}Sn)	6553 (^{119}Sn)	9.0	82.36 (^{119}Sn)	40.17 (^{119}Sn)	247.4	56.76
							221 (^{205}Tl)	6474 (^{117}Sn)	6.4	9.86 (^{205}Tl)	2.24 (^{205}Tl)		
$TlPbTe_3^{3-}$	en/ ethylamine[e]	0		3483	2188	−944	280 (^{207}Pb)	13086 (^{205}Tl)	8.9	34.85 (^{207}Pb)	7.86 (^{207}Pb)	883.2	93.77
							307 (^{205}Tl)	12962 (^{203}Tl)	5.6	13.70 (^{205}Tl)	3.11 (^{205}Tl)		
$Pb_2Te_3^{2-}$	en	24			1727	−928	1074		6.5	161.1	36.36		
$Sn_2Se_3^{2-}$	en	24	421			12	397	1514	9.0	46.0	28.0	89.6	44.1
$SnPbSe_3^{2-}$	en	3	528		3439	−42	415 (^{119}Sn)	1145	9.2	48.1 (^{119}Sn)	29.2 (^{119}Sn)	120.9	27.6
							153 (^{207}Pb)		7.2	31.6 (^{207}Pb)	8.89 (^{207}Pb)		
$Pb_2Se_3^{2-}$	en	31			3302	−99	153		7.2	31.6	8.89		
$Tl_2Se_2^{2-}$	en	0	7689				2265	4506	10.4	167.9	47.52	110.1	11.90
	NH_3	−70	7595			372	2261	3602	10.4	167.6	47.44	88.01	9.56
$Tl_2Te_2^{2-}$	en	0	8175				4004	6337	8.7	178.7	40.60	154.8	16.74
	NH_3	−70	8050				3989	7591	8.7	178.0	40.44	185.5	20.05

[a] Present work. [b] From ref 4. [c] From ref 5. [d] From ref 27. [e] The percentage of ethylamine, 6.7 mol %, was determined from the ^{1}H NMR spectrum.

Table 5. Natural Abundance Isotopomers and Subspectra Used To Simulate the ^{119}Sn, ^{125}Te, ^{205}Tl, and ^{207}Pb NMR Spectra of the $TlMTe_3^{3-}$ Anions (M = Sn, Pb)

	total intensity[a,b] in the spectrum of			multiplicity[a,c] of subspectrum		
isotopomer	^{205}Tl	*M	^{125}Te	^{205}Tl	*M	^{125}Te
$^{205}TlSnTe_3^{3-}$	0.674			S		
$^{205}TlPbTe_3^{3-}$	0.623			S		
$^{205}Tl^{119}SnTe_3^{3-}$	0.069	0.567		D_A	D_A	
$^{205}Tl^{207}PbTe_3^{3-}$	0.182	0.567		D_A	D_A	
$^{205}Tl^{117}SnTe_3^{3-}$	0.061			D_B		
$^{205}TlSn^{125}TeTe_2^{3-}$	0.152		0.591	d_A		d_B
$^{205}TlPb^{125}TeTe_2^{3-}$	0.140		0.546	d_A		d_B
$^{205}Tl^{119}Sn^{125}TeTe_2^{3-}$	0.016	0.128	0.061	D_A/d_A	D_A/d_C	d_B/d_D
$^{205}Tl^{207}Pb^{125}TeTe_2^{3-}$	0.041[d]	0.128	0.159	D_A/d_A	D_A/d_C	d_B/d_C
$^{205}Tl^{117}Sn^{125}TeTe_2^{3-}$	0.014[d]		0.054	D_B/d_A		d_B/d_D
$^{203}Tl^{119}SnTe_3^{3-}$		0.237			D_C	
$^{203}Tl^{207}PbTe_3^{3-}$		0.237			D_C	
$^{203}Tl^{119}Sn^{125}TeTe_2^{3-}$		0.054[d]	0.025		D_C/d_C	d_B/d_D
$^{203}Tl^{207}Pb^{125}TeTe_2^{3-}$		0.054[d]	0.067[d]		D_C/d_C	d_B/d_C
$^{203}TlSn^{125}TeTe_2^{3-}$			0.247			d_B
$^{203}TlPb^{125}TeTe_2^{3-}$			0.228			d_B
$^{203}Tl^{117}Sn^{125}TeTe_2^{3-}$			0.022[d]			d_B/d_D

[a] *M denotes ^{119}Sn or ^{207}Pb. [b] Natural abundances of the spin-$^1/_2$ nuclides used to calculate isotopomer abundances were taken from ref 31: ^{117}Sn, 7.61%; ^{119}Sn, 8.58%; ^{125}Te, 6.99%; ^{203}Tl, 29.5%; ^{205}Tl, 70.5%; ^{207}Pb, 22.6%. The natural abundances of ^{115}Sn (0.35%) and ^{123}Te (0.87%) are too low to contribute detectable isotopomer subspectra and are combined with the spinless tin and tellurium nuclides, respectively. [c] S denotes a singlet; D_A, D_B, and D_C denote DOUBLETS arising from $J(^{205}\text{Tl}-\text{*M})$, $J(^{205}\text{Tl}-^{117}\text{Sn})$, and $J(\text{*M}-^{203}\text{Tl})$, respectively; and d_A, d_B, d_C, and d_D denote doublets arising from $J(^{205}\text{Tl}-^{125}\text{Te})$, unresolved $J(^{125}\text{Te}-^{203,205}\text{Tl})$, $J(\text{*M}-^{125}\text{Te})$, and unresolved $J(^{125}\text{Te}-^{117,119}\text{Sn})$, respectively. The symbols D/d generally denote DOUBLETS-of-doublets. For example, the symbol D_A/d_A denotes a DOUBLETS-of-doublets that results from $J(^{205}\text{Tl}-\text{*M})$ which, in turn, is split into a doublet by $J(^{205}\text{Tl}-^{125}\text{Te})$. [d] Isotopomers having multiplet line intensities below 0.014 are too low to be observed and are not included in the summations of the simulated spectra.

with an anion site symmetry of D_3 and give rise to five Raman active vibrational bands, $\nu_1-\nu_4$ and ν_6, which are not split in the Raman spectrum. In the infrared spectrum, $\nu_3-\nu_6$ are active and each band is split into gerade and ungerade components.

The observation of six vibrational bands in the Raman spectrum of the $Pb_2S_3^{2-}$ anion in (2,2,2-crypt-K^+)$_2Pb_2S_3^{2-}$·0.5en (Figure 4), including the formally Raman inactive, but infrared active A_2'' mode, is in agreement with the factor-group analysis. Four and five Raman-active bands predicted from the factor-group analysis were observed for the $Sn_2Se_3^{2-}$ and $Pb_2Se_3^{2-}$ anions in (2,2,2-crypt-K^+)$_2M_2Se_3^{2-}$, respectively. With the exception of $\nu_2(A_1')$ in $Pb_2Se_3^{2-}$ and $\nu_4(E')$ in $Sn_2Se_3^{2-}$, which exhibit shoulders, the predicted factor-group splittings of the Raman bands were too small to be resolved. Contrary to $Pb_2Se_3^{2-}$, $\nu_6(E'')$ was not resolved in $Sn_2Se_3^{2-}$ and is assumed to overlap with $\nu_2(A_1')$. Five and four Raman active bands predicted from the factor-group analysis were observed for the $Sn_2Te_3^{2-}$ and $Pb_2Te_3^{2-}$ anions, respectively, in (2,2,2-crypt-K^+)$_2M_2Te_3^{2-}$. In addition, a weak band assigned to the formally Raman inactive $\nu_5(A_2'')$ mode was observed for the $Pb_2Te_3^{2-}$ anion. The vibrational assignments for the $M_2Ch_3^{2-}$ anions are those of the gas-phase $M_2Ch_3^{2-}$ anions under D_{3h} symmetry, with the exception that the formally infrared active and Raman inactive $\nu_5(A_2'')$ mode is also observed in the Raman spectra of $Pb_2S_3^{2-}$, $M_2Se_3^{2-}$, and $Pb_2Te_3^{2-}$. The calculated frequencies for $\nu_2(A_1')$ and $\nu_6(E'')$ are very similar in the case of the $Pb_2Ch_3^{2-}$ anions. The stronger peak is assigned to $\nu_2(A_1')$ because deformation modes are generally expected to be weaker than stretching modes. A medium intensity peak was also observed at 75 cm^{-1} in the Raman spectrum of $Pb_2Te_3^{2-}$ and is tentatively assigned to a lattice mode rather than to the $\nu_2(A_1')$ or $\nu_6(E'')$ modes because factor-group splitting is not predicted for either $\nu_2(A_1')$ or $\nu_6(E'')$.

For (2,2,2-crypt-K^+)$_3TlPbTe_3^{3-}$·2en, correlation of the free anion symmetry of $TlPbTe_3^{3-}$ (C_{3v}) to the anion site symmetry (C_1) and the unit cell symmetry, C_{2h} (space group $P2_1/c$) reveals that all six vibrational modes of the free anion are split into A_g and B_g components in the Raman spectrum and into A_u and B_u components in the infrared spectrum; however, no splittings could be resolved in the Raman spectrum. The vibrational assignments of the $TlPbTe_3^{3-}$ anion are therefore given for the free anion under C_{3v} symmetry where $\nu_1(A_1)$, $\nu_2(A_1)$, $\nu_3(A_1)$, and $\nu_4(E)$ can be assigned with confidence.

The experimental Raman values are in good agreement with the values calculated at both the local (LDFT) and nonlocal (NLDFT) density functional theory levels. The $Sn_2Se_3^{2-}$ and $Sn_2Te_3^{2-}$ anion modes were shifted to higher frequency relative to those of the $Pb_2Se_3^{2-}$ and $Pb_2Te_3^{2-}$ anions, respectively. High-frequency shifts were observed for the $Sn_2Ch_3^{2-}$ and $Pb_2Ch_3^{2-}$ anions upon substitution of lighter chalcogen atoms

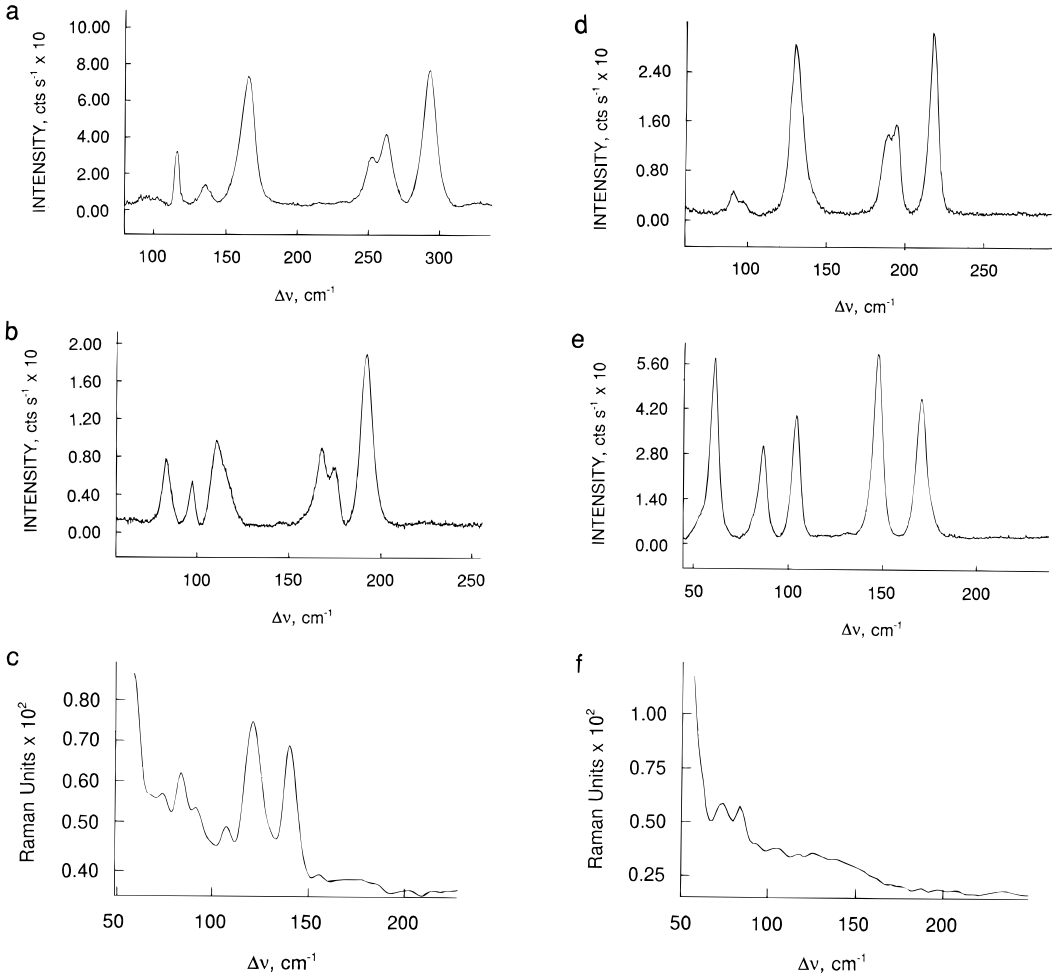

Figure 4. Raman spectra of the (a) $Pb_2S_3^{2-}$, (b) $Pb_2Se_3^{2-}$, (c) $Pb_2Te_3^{2-}$, (d) $Sn_2Se_3^{2-}$, (e) $Sn_2Te_3^{2-}$, and (f) $TlPbTe_3^{3-}$ anions in (2,2,2-crypt-K^+)$_2M_2Ch_3^{2-}$ (M = Sn, Pb; Ch = S, Se, Te), (2,2,2-crypt-K^+)$_2Pb_2S_3^{2-}$·0.5en, and (2,2,2-crypt-K^+)$_3TlPbTe_3^{3-}$·2en were recorded in a glass capillary on powdered microcrystalline samples at room temperature by using 514.5 ($Sn_2Se_3^{2-}$, $Pb_2S_3^{2-}$), 647.1 ($Sn_2Te_3^{2-}$, $Pb_2Se_3^{2-}$), and 1064 ($Pb_2Te_3^{2-}$, $TlPbTe_3^{3-}$) nm excitation.

for both experimental and calculated frequencies and may be attributed to the reduced mass effect (Table 6). Similar reduced mass effects are observed for the calculated frequencies of $SnPbSe_3^{2-}$ where the frequency trend is $Sn_2Se_3^{2-} \rightarrow SnPbSe_3^{2-} \rightarrow Pb_2Se_3^{2-}$. The experimental and calculated vibrational frequencies of $TlPbTe_3^{3-}$ occur at lower values than those of $Pb_2Te_3^{2-}$ and may arise from more polar bonding in the more negatively charged $TlPbTe_3^{3-}$ anion. The anion charge and reduced mass effects are also reflected in the lower calculated frequencies of $TlSnTe_3^{3-}$ relative to those of $Sn_2Te_3^{2-}$ but are greater than those of $TlPbTe_3^{3-}$.

Computational Results. The results of the density functional theory calculations at the local (LDFT) and nonlocal (NLDFT) levels for the $M_2Ch_3^{2-}$, $TlMTe_3^{3-}$ (M = Sn, Pb; Ch = S, Se, Te) and $SnPbSe_3^{2-}$ anions are summarized in Tables 3 and 6−10. The vibrational frequencies and their assignments are discussed in the section "Vibrational Spectra of the $M_2Ch_3^{2-}$ (M = Sn, Pb; Ch = S, Se, Te) and $TlPbTe_3^{3-}$ Anions".

(a) Geometries. The different calculations give varying but good agreement with experiment for the energy-minimized trigonal bipyramidal geometries. The geometries derived for the $Sn_2Ch_3^{2-}$ anions give the best agreement with the experimental values at the LDFT level when all electron basis sets are used for the Sn and Ch atoms. In general, the M−M, M−Ch, and Ch−Ch distances are predicted to be longer than the experimental ones, except for $Sn_2Te_3^{2-}$ where the calculated Sn−Sn value is in excellent agreement with the experimental value. As expected, nonlocal corrections lead to lengthening of all of the bonds. The calculated Sn−Ch−Sn and Ch−Sn−Ch bond angles are within 1° at the local DZVP/DZVP level. Nonlocal corrections somewhat reduce the Sn−Ch−Sn bond angles and increase the Ch−Sn−Ch bond angles. The local ECP results for the Sn clusters are similar to the local all-electron ones except that the calculated Sn−Te bond length is now ∼0.1 Å longer than the experimental value.

The geometries derived for the $Pb_2Ch_3^{2-}$ anions at the ECP level give the best agreement for the Pb−Pb and Pb−Ch bond distances although the calculated Pb−Pb distances are somewhat shorter than the experimental ones. Similar calculations for the Pb_9^{3-} and Pb_9^{4-} anions also underestimated the Pb−Pb distances.[17] The experimentally observed increase in Pb−Pb distance with increasing size of Ch is reproduced by the calculations. The local PP/DZVP calculations also reproduce this trend even though the Pb−Pb distances are too short by ∼0.15 Å, but the local PP/PP calculations fail to reproduce the trend. These results differ from our prior calculations on the $Tl_2Ch_2^{2-}$ (Ch = Se and/or Te) anions where the all pseudopotential calculations gave better results than the mixed PP/basis set results.[27] Overall, the nonlocal calculations give longer bond lengths than the local calculations. The calculated Pb−Ch−Pb and Ch−Pb−Ch bond angles are also well reproduced at the ECP level, showing the trends observed experimentally, i.e., Pb−S−Pb > Pb−Se−Pb > Pb−Te−Pb and S−Pb−S < Se−Pb−Se < Te−Pb−Te.

Table 6. Experimental Raman and Calculated Vibrational Frequencies for the $M_2Ch_3^{2-}$ (M = Sn, Pb; Ch = Se, Te), $Pb_2S_3^{2-}$, and $TlPbTe_3^{3-}$ Anions in $(2,2,2\text{-crypt-}K^+)_2Sn_2Ch_3^{2-}$ (Ch = Se, Te), $(2,2,2\text{-crypt-}K^+)_2Pb_2Ch_3^{2-}\cdot 0.5en$ (Ch = S, Se), $(2,2,2\text{-crypt-}K^+)_2Pb_2Te_3^{2-}$, and $(2,2,2\text{-crypt-}K^+)_2Pb_2Ch_3^{2-}\cdot 2en$ and Calculated Vibrational Frequencies for the $SnPbSe_3^{2-}$ and $TlSnTe_3^{3-}$ Anions[a]

	$Sn_2S_3^{2-}$		$Sn_2Se_3^{2-}$			$Sn_2Te_3^{2-}$		
	DZVP/DZVP[b]			DZVP/DZVP[b]			DZVP/DZVP[b]	
assignt[c]	LDFT	NLDFT	expt[d]	LDFT	NLDFT	expt[d]	LDFT	NLDFT
$\nu_1(A_1')$	321 (0)	301 (0)	217 (100)	220 (0)	214 (0)	171 (76)	179 (0)	167 (0)
$\nu_2(A_1')$	164 (0)	159 (0)	130 (94)	121 (0)	128 (0)	88 (50)	84 (0)	82 (0)
$\nu_3(E')$	293 (156)	275 (165)	194 (50)	194 (80)	194 (108)	148 (100)	158 (64)	145 (67)
$\nu_4(E')$	142 (10)	139 (10)	97 (7), sh 90 (13)	85 (0)	86 (0)	62 (98)	60 (0)	58 (0)
$\nu_5(A_2'')$	275 (97)	261 (95)	189 (45)	191 (30)	192 (29)	*f*	154 (10)	145 (9)
$\nu_6(E'')$	187 (0)	169 (0)	*e*	130 (0)	122 (0)	105 (67)	112 (0)	100 (0)

	$Pb_2S_3^{2-}$			$Pb_2Se_3^{2-}$			$Pb_2Te_3^{2-}$		
		PP/DZVP2[b]			PP/DZVP[b]			PP/DZVP[b]	
assignt[c]	expt[d]	LDFT	NLDFT	expt[d]	LDFT	NLDFT	expt[d]	LDFT	NLDFT
$\nu_1(A_1')$	292 (100)	292 (0)	280 (0)	192 (100)	197 (0)	187 (0)	141 (91)	154 (0)	147 (0)
$\nu_2(A_1')$	165 (94)	141 (0)	150 (0)	117 (23), sh 111 (49)	102 (0)	99 (0)	85 (41)	89 (0)	87 (0)
$\nu_3(E')$	262 (52)	262 (215)	248 (233)	175 (34)	182 (107)	170 (109)	122 (100)	142 (74)	134 (75)
$\nu_4(E')$	116 (40)	116 (10)	114 (10)	84 (37)	68 (4)	68 (4)	*g*	44 (0)	46 (0)
$\nu_5(A_2'')$	252 (36)	237 (64)	229 (60)	168 (45)	154 (18)	146 (17)	109 (19)	117 (6)	111 (6)
$\nu_6(E'')$	136 (16)	142 (0)	130 (0)	98 (20)	102 (0)	91 (0)	93 (23)	82 (0)	74 (0)
lattice mode							75 (15)		

	$TlPbTe_3^{3-}$			$SnPbSe_3^{2-}$		$TlSnTe_3^{3-}$
		PP/PP/DZVP2[b]		PP/PP/DZVP2[b]		ECP/ECP/ECP[b]
assignt[h]	expt[d]	LDFT	NLDFT	LDFT	NLDFT	LDFT
$\nu_1(A_1)$	125 (35)	131 (0)	124 (0)	209 (1)	198 (1)	143 (0)
$\nu_2(A_1)$	84 (100)	91 (3)	86 (3)	177 (19)	168 (18)	93 (4)
$\nu_3(A_1)$	73 (80)	85 (10)	82 (0)	110 (2)	108 (0)	75 (1)
$\nu_4(E)$	104 (25)	117 (55)	110 (58)	187 (95)	176 (98)	120 (77)
$\nu_5(E)$	*g*	50 (0)	52 (0)	118 (0)	10 (2)	54 (8)
$\nu_6(E)$	*g*	46 (10)	3 (7)	76 (1)	76 (1)	43 (0)

[a] Frequencies in cm^{-1}. [b] Infrared intensities, in km mol^{-1}, are given in parentheses. [c] Although the assignments are for the gas-phase $M_2Ch_3^{2-}$ anions under D_{3h} symmetry, the calculated symmetry is only approximately D_{3h}. [d] Values in parentheses denote relative Raman intensities. [e] Likely overlaps with intense $\nu_2(A_1')$. [f] Likely overlaps with intense $\nu_3(E')$. [g] Not observed. [h] The assignments are for the gas-phase $TlMTe_3^{3-}$ and $SnPbSe_3^{2-}$ anions under C_{3v} symmetry.

The calculated Tl−Pb bond length for the $TlPbTe_3^{3-}$ anion is smaller than the experimental value by ∼0.15 Å at all levels. The average Tl/Pb−Te distance is in good agreement with experiment at all levels, with the PP/DZVP2 calculations providing the best agreement with experiment. The Te−Tl/Pb−Te angle is overestimated when compared to experiment which is consistent with the calculated Ch−M−Ch angles of the $M_2Ch_3^{2-}$ anions. The Te−Tl−Te angles of $TlMTe_3^{3-}$ are predicted to be significantly larger than the Te−M−Te angles by ∼10° and contrasts with the $SnPbSe_3^{2-}$ anion where the difference between the calculated Se−Sn−Se and Se−Pb−Se angles is considerably smaller.

(b) Charge Distributions and Bonding. The anion charge distribution varies considerably from $Sn_2Ch_3^{2-}$ to $Pb_2Ch_3^{2-}$ and among the $TlMTe_3^{3-}$ and $SnPbSe_3^{2-}$ anions (Table 7). The Mülliken charges are discussed first. In $Sn_2Ch_3^{2-}$, the anion negative charge is localized on the more electronegative chalcogen atom and is almost equally shared between the Sn and the S in $Sn_2S_3^{2-}$. The larger ionicity predicted for the $Sn_2Se_3^{2-}$ and $Sn_2Te_3^{2-}$ anions does not follow chalcogen electronegativity trends. In $Tl_2Ch_2^{2-}$, the charge was found to be localized on the more electronegative Ch atoms but was comparable for Se (−0.71) and Te (−0.68).[27] The bonding in the $Pb_2Ch_3^{2-}$ anion series is predicted to be significantly more ionic than in $Sn_2Ch_3^{2-}$ and is in qualitative agreement with electronegativity expectations ($\chi_{Sn} = 1.80$, $\chi_{Pb} = 1.87$ and $\chi_{Tl} = 1.62$; Allred−Rochow values for Sn(II), Pb(II) and Tl(I) scaled to the Pauling values).[36] For $Pb_2Ch_3^{2-}$, a much more ionic bonding environment is predicted with the Pb being quite positive (0.25) and the chalcogen being quite negative (∼−0.85). There is no apparent variation of the negative charge on the chalcogen with the electronegativity. The negative charge is also localized on the more electronegative chalcogen atoms in the mixed anions. The charges on Sn are consistently more negative than those on Pb over the $M_2Ch_3^{2-}$ series including $SnPbSe_3^{2-}$, and opposite to the anticipated trend based on the relative electronegativities of Sn(II) and Pb(II). A similar trend is found for Sn and Pb of the $TlMTe_3^{3-}$ anions. The $TlPbTe_3^{3-}$ anion exhibits the most ionic bonding at the PP/PP/DZVP2 level with significantly greater charge on Tl. The charge distributions are similar for both $TlMTe_3^{3-}$ anions at the all ECP level and, unlike the PP/PP/DZVP2 distributions, follow electronegativity trends.

The calculated Mayer valencies[37] for $Sn_2Ch_3^{2-}$ give values of 3 for Sn and 2 for the Ch atoms (Table 8), consistent with three Ch atoms covalently bonded to each Sn atom, however, the agreement is not as good at the PP/DZVP level. The

(36) Huheey, J. E. *Inorganic Chemistry: Principles of Structure and Reactivity*, 4th ed.; Harper Collins College Publishers: New York, 1993; pp 187−190.

(37) Mayer, I. *Chem. Phys. Lett.* **1983**, *97*, 270; *Theor. Chim. Acta* **1985**, *67*, 315; *Int. J. Quantum Chem.* **1986**, *29*, 73.

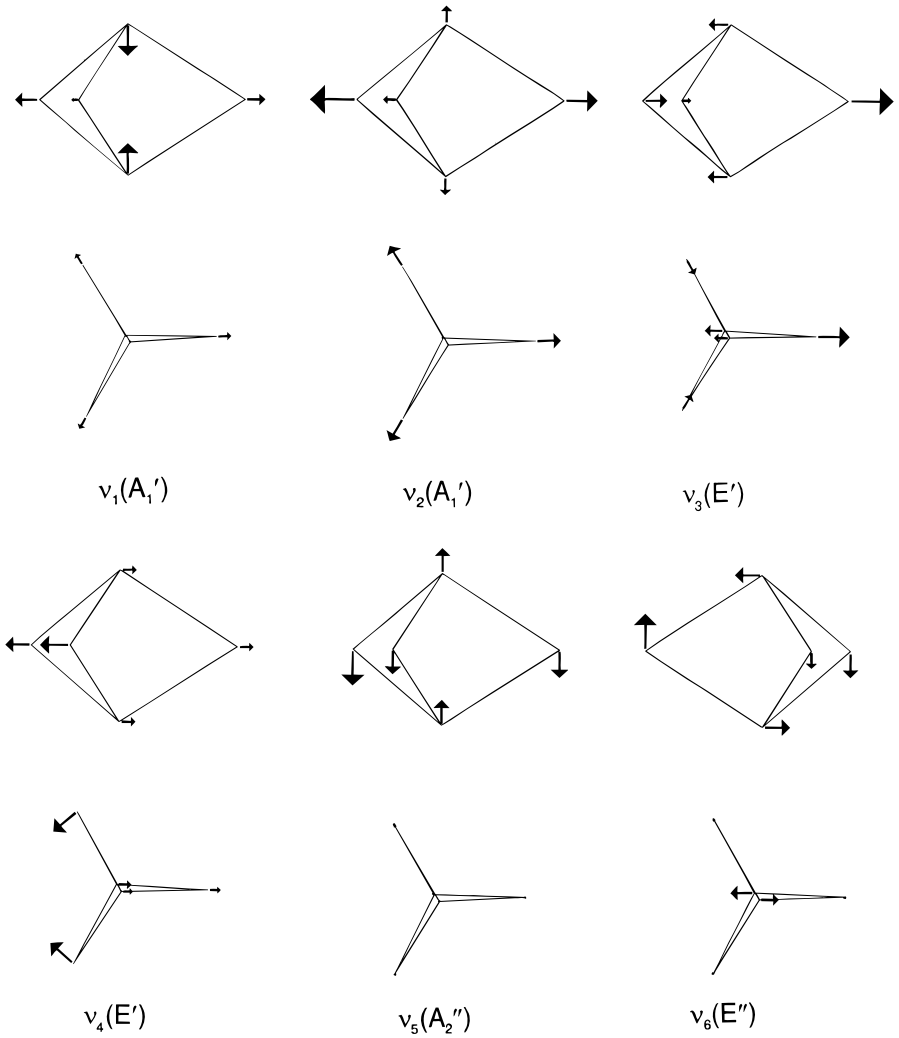

Figure 5. Vibrational modes of the trigonal bipyramidal $M_2S_3^{2-}$, $Sn_2Te_3^{2-}$, and $Pb_2Se_3^{2-}$ (M = Sn, Pb) anions (side-on and top-on views). The $Sn_2Se_3^{2-}$ and $Pb_2Te_3^{2-}$ anions have the orders of their two A_1' modes reversed.

Table 7. Mülliken Charges (e) for the $M_2Ch_3^{2-}$, $TlMTe_3^{3-}$ (M = Sn, Pb; Ch = S, Se, Te), and $SnPbSe_3^{2-}$ Anions

	$Sn_2S_3^{2-}$		$Sn_2Se_3^{2-}$		$Sn_2Te_3^{2-}$	
	DZVP/DZVP		DZVP/DZVP		DZVP/DZVP	
atom	LDFT	NLDFT	LDFT	NLDFT	LDFT	NLDFT
M	−0.30	−0.19	−0.18	−0.09	−0.14	−0.07
Ch	−0.36	−0.54	−0.54	−0.72	−0.57	−0.62

	$Pb_2S_3^{2-}$			$Pb_2Se_3^{2-}$			$Pb_2Te_3^{2-}$		
	PP/DZVP2		PP/PP	PP/DZVP		PP/PP	PP/DZVP		PP/PP
atom	LDFT	NLDFT	LDFT	LDFT	NLDFT	LDFT	LDFT	NLDFT	LDFT
M	0.23	0.26	0.02	0.28	0.29	0.12	0.27	0.13	0.08
Ch	−0.82	−0.84	−0.68	−0.85	−0.86	−0.74	−0.85	−0.75	−0.72

	$TlPbTe_3^{3-}$			$SnPbSe_3^{2-}$			$TlSnTe_3^{3-}$	
	PP/PP/DZVP2		ECP/ECP/ECP		PP/DZVP/DZVP			ECP/ECP/ECP
atom	LDFT	NLDFT	LDFT	atom	LDFT	NLDFT	atom	LDFT
Tl	−0.38	−0.34	0.23	Pb	0.28	0.28	Tl	0.17
Pb	−0.09	−0.03	−0.17	Sn	−0.14	−0.06	Sn	−0.12
Te	−0.84	−0.88	−1.02	Se	−0.71	−0.74	Te	−1.02

calculated Mayer valencies for the $Pb_2Ch_3^{2-}$ series give values of about 2.4 for Pb and about 1.6 for Ch (Table 8) and reflect the higher ionic component to the bonding. Similar values are calculated for $TlPbTe_3^{3-}$ and $SnPbSe_3^{2-}$. The calculated Pb−Ch Mayer bond orders[37] (0.72−0.83) are significantly smaller than the Sn−Ch values (0.82−0.96) and also reflect more ionic Pb−Ch bonds (Table 8). In $SnPbSe_3^{2-}$, the bond order for Pb−Se (0.75) is found to be smaller than that of Sn−Se (0.91) which follows the trend observed for M−Se in $Pb_2Se_3^{2-}$ (0.19) and $Sn_2Se_3^{2-}$ (0.27). There are weak interactions between the M

Table 8. Mayer Valencies and Mayer Bond Orders in the $M_2Ch_3^{2-}$ (M = Sn, Pb; Ch = S, Se, Te), $TlPbTe_3^{3-}$, and $SnPbSe_3^{2-}$ Anions

	$Sn_2Ch_3^{2-}$						$Pb_2Ch_3^{2-}$					
	LDFT						LDFT			NLDFT		
	DZVP/DZVP			PP/DZVP			PP/DZVP			PP/DZVP		
	S	Se	Te	S	Se	Te	S[a]	Se	Te	S[a]	Se	Te
valencies												
M	3.20	3.01	2.97	2.65	2.64	2.87	2.44	2.41	2.44	2.41	2.39	2.42
Ch	1.97	1.87	1.87	1.87	1.69	2.06	1.65	1.60	1.59	1.63	1.58	1.58
bond orders												
M−M	0.32	0.27	0.27	0.17	0.21	0.25	0.13	0.19	0.28	0.14	0.20	0.29
M−Ch	0.96	0.91	0.90	0.82	0.81	0.88	0.77	0.74	0.72	0.76	0.73	0.71
Ch···Ch	0.03	0.02	0.04	0.03	0.03	0.15	0.06	0.06	0.08	0.06	0.06	0.08

	$TlPbTe_3^{3-}$			$SnPbSe_3^{2-}$			
valencies	LDFT	bond orders	LDFT	valencies	LDFT	bond orders	LDFT
Tl	2.19	Tl−Pb	0.22	Sn	2.91	Sn−Pb	0.19
Pb	2.96	Tl−Te	0.64 × 2; 0.69	Pb	2.44	Sn−Se	0.91
Te	1.85 × 2; 1.86	Pb−Te	0.93 × 2; 0.89	Se	1.74	Pb−Se	0.75

[a] DZVPZ basis set on S.

Table 9. Natural Atomic Orbital Populations for the Valence Atomic Orbitals of the $M_2Ch_3^{2-}$, $TlMTe_3^{3-}$ (M = Sn, Pb; Ch = S, Se, Te), and $SnPbSe_3^{2-}$ Anions and Their Charges

	$Sn_2Ch_3^{2-}$				$Pb_2Ch_3^{2-}$			
	orbital population				orbital population		
atomic orbital	S	Se	Te	atomic orbital	S	Se	Te
Sn (s)	1.73	1.76	1.81	Pb (s)	1.85	1.87	1.89
Sn (p_x)	0.46	0.47	0.57	Pb (p_x)	0.48	0.47	0.55
Sn (p_y)	0.46	0.47	0.57	Pb (p_y)	0.48	0.47	0.55
Sn (p_z)	0.84	0.83	0.82	Pb (p_z)	0.75	0.72	0.69
Ch (s)	1.87	1.88	1.88	Ch (s)	1.89	1.91	1.90
Ch (p_y)	1.73	1.90	1.90	Ch (p_y)	1.86	1.90	1.90
Ch (p_x)	1.67	1.58	1.45	Ch (p_x)	1.64	1.56	1.46
Ch (p_z)	1.58	1.59	1.56	Ch (p_z)	1.56	1.61	1.60
	charge				charge		
Sn	0.49	0.46	0.22	Pb	0.44	0.48	0.30
Ch	−0.99	−0.98	−0.81	Ch	−0.96	−0.99	−0.87

atomic orbital	orbital population	atomic orbital	orbital population	atomic orbital	orbital population		charge
			$SnPbSe_3^{2-}$				
Sn (s)	1.77	Pb (s)	1.86	Se (s)	1.90	Sn	0.46
Sn (p_x)	0.47	Pb (p_x)	0.47	Se (p_x)	1.90	Pb	0.48
Sn (p_y)	0.47	Pb (p_y)	0.47	Se (p_y)	1.50	Se	−0.98
Sn (p_z)	0.82	Pb (p_z)	0.72	Se (p_z)	1.60		
			$TlPbTe_3^{3-}$				
Tl (s)	1.92	Pb (s)	1.89	Te (s)	1.90	Pb	0.24
Tl (p_x)	0.33	Pb (p_x)	0.56	Te (p_x)	1.81	Tl	−0.07
Tl (p_y)	0.33	Pb (p_y)	0.56	Te (p_y)	1.61	Te	−1.06
Tl (p_z)	0.48	Pb (p_z)	0.75	Te (p_z)	1.73		
			$TlSnTe_3^{3-}$				
Tl (s)	1.91	Sn (s)	1.82	Te (s)	1.89	Sn	0.18
Tl (p_x)	0.33	Sn (p_x)	0.57	Te (p_x)	1.91	Tl	−0.05
Tl (p_y)	0.33	Sn (p_y)	0.57	Te (p_y)	1.52	Te	−1.04
Tl (p_z)	0.33	Sn (p_z)	0.57	Te (p_z)	1.71		

atoms in both anion series and in the mixed anions (bond order, 0.17−0.32 for Sn−Sn, 0.13−0.28 for Pb−Pb, 0.22 for Tl−Pb, and 0.19 for Sn−Pb) and between the Ch atoms (bond order, 0.02−0.15 for $Sn_2Ch_3^{2-}$ and 0.06−0.15 for $Pb_2Ch_3^{2-}$). It is noteworthy that even though the calculated Sn−Sn distances in $Sn_2Ch_3^{2-}$ are larger than the experimental values, significant Sn−Sn bond orders are calculated for these anions. In the case of the $Tl_2Se_2^{2-}$ and $Tl_2Te_2^{2-}$ anions, bond orders were calculated from the experimental geometries in order to show that the calculated Tl−Tl interactions were not exaggerated because the predicted Tl−Tl distances were shorter than the experimental values.[27] Moreover, the M−M interactions in the $M_2Ch_3^{2-}$ anion series are predicted to increase in the order Te > Se > S despite the observed and calculated increase in the M−M distance with increasing Ch atom size.

The NBO atomic populations (Table 9) show more ionicity as compared to the Mülliken charges. The sulfur and selenium anions have about the same charges for the Sn and Pb anions with a positive charge of about 0.45 e on M and a negative charge of about −1.0 e on Ch. This is quite different than what the Mülliken charge distribution predicted for the $Sn_2Ch_3^{2-}$ anions where it was found to carry some negative charge. The Te anions are both predicted to be less ionic with a positive charge of 0.22 e on the Sn and 0.30 e on the Pb. The values obtained for the mixed systems also differ from the Mülliken charges, with all the negative charge on the chalcogen atoms.

The NBO analyses of the mixed $SnPbSe_3^{2-}$ and $TlMTe_3^{3-}$ anions show that the bonding is essentially unchanged from that in the $M_2Se_3^{2-}$ and $M_2Te_3^{2-}$ anions, respectively. The Tl−Te bonds in both mixed anions are similar to each other and are more ionic than the Sn−Te and Pb−Te bonds. We also note that in all the anions, the valence s orbital populations on M/Tl are 1.73−1.92, consistent with the M−M/Tl−M interactions essentially arising from s−s overlap. Within each $M_2Ch_3^{2-}$ series, the s orbital population on M increases with increasing size of Ch. The highest metal s orbital populations are found for the mixed $TlMTe_3^{3-}$ anions with a higher value for Tl. In $TlSnTe_3^{3-}$ and $TlPbTe_3^{3-}$, the NBO charge analyses show that the Tl atom is more negative than the M atom. This is consistent with the Mülliken charge analysis derived from the PP calculations for $TlPbTe_3^{3-}$ but not with that derived from the ECP calculations for both $TlMTe_3^{3-}$ anions.

The NBO analyses were used to further assess the bonding in the $M_2Ch_3^{2-}$ anion series (Table 10). The analysis shows two-center M−Ch (Tl−Te) bonds with populations of 1.95−1.97 (1.91). The remaining bond population is in the σ^* orbital. We note that for $TlPbTe_3^{3-}$, the NBO analysis places more electrons in both the Pb−Te bonding and antibonding orbitals than in the corresponding Tl−Te orbitals. The M−Ch (Tl−Te) bond has about 78 (85%) of the two electrons on Ch (Te) and about 22% (15%) on M (Tl). The bonding is predominantly p in character with about 93−96% (97%) p-character on M (Tl) and about 86−92% (93%) p character on Ch (Te) (Table 10). The remaining valence electrons are found in lone pairs, with one lone pair on each metal atom and two lone pairs on each chalcogen atom. There is essentially a doubly occupied lone pair of high s orbital character ($sp^{0.1}$) on each M (Tl) atom (ca. 82−91% (94%)) and each Ch (Te) atom (ca. 73−91% (83−84%)). The s-orbital character of the Ch atom lone pair increases with increasing size of the Ch atom. Each Ch (Te) atom also possesses a lone pair of pure p character. As in the case of the $Tl_2Se_2^{2-}$, Tl_2SeTe^{2-}, and $Tl_2Te_2^{2-}$ anions,[27] the NBO analysis did not assign any orbital to weak M−M, Tl−M, or Ch−Ch interactions, but to lone pairs. However, this is not inconsistent with the Mayer analysis which considers total overlap of orbitals between atoms. In $TlMTe_3^{3-}$, there is more s character on M and Ch in the M−Te bond when compared to the Tl−Te bond. In $SnPbSe_3^{2-}$, the percentage of s character is higher on Sn and Se in the Sn−Se bond than on Pb and Se in the Pb−Se bond. The natural atomic orbital occupancies show that the valence s orbitals are missing 0.20 to 0.25 e on the Sn from being doubly occupied and 0.12 e from the s orbital on the Ch from being doubly occupied. The p_z orbital on M along the M−M axis has about 0.7−0.8 e, and the other p orbitals on the Sn have 0.5−0.6 e. The p orbitals on the Ch are missing about 0.4 e in the out-of-plane orbital. There is somewhat less density missing for the in-plane p_y orbitals from being doubly occupied, with the in-plane p_x orbital showing missing density comparable to that missing from the p_z orbital. These populations are consistent with the form of the lone pairs described by the NBO analysis.

The LUMO and valence-MO's for $Pb_2S_3^{2-}$ are shown in Figure 6 and are similar to those of $Pb_2Ch_3^{2-}$ (Ch = Se, Te), $Sn_2Ch_3^{2-}$ (Ch = S, Se, Te), and $TlPbTe_3^{3-}$.[38] The LUMO (A_2'') is composed predominantly of an antibonding sp hybrid (excess s character) on the metal atoms directed along the M−M axis with very small antibonding interactions with the out-of-plane p orbital on the chalcogens. The HOMO (A_2') is the antibonding interaction of the in-plane (*xy* trigonal plane) lone pair p orbitals on the Ch atoms. The NHOMO (A_2'') is the antibonding interaction of the out-of-plane lone pair p orbitals on the Ch atoms. The next highest orbitals are the in-plane lone pairs on Ch (E′) and the out-of-plane lone pairs on Ch (E″) with the E′ orbitals higher in energy than the E″ orbitals. The seventh and eighth highest orbitals are of E′ symmetry and involve Ch−Ch bonding along the edge of the trigonal plane. The ninth orbital (A_1') is the chalcogen sp orbitals bonding through the center (in the trigonal plane) of the cluster plus an antibonding sp_z hybrid-type orbital on each M atom. The tenth orbital (A_1') is an M−M bonding type orbital. The interaction is greatest for the Sn derivatives and arises mostly from the overlap of the valence s orbitals on the M atoms with some antibonding character on the Ch atoms. The eleventh orbital (A_2'') is the antibonding interaction of the s orbitals on the M atoms and is lower in energy than the bonding interaction. The next to lowest energy (E′) valence orbitals and the lowest energy (A_1') valence orbital correspond to the bonding and antibonding, respectively, of the doubly occupied valence s orbitals on the chalcogens.

(c) NMR Parameters. The extreme high-frequency ^{207}Pb chemical shifts of $Pb_2Se_xTe_{3-x}^{2-}$,[4] $Ph_3Pb_3^-$,[39] and $Pb[N(SiMe_3)_2]_2$[40] relative to $(CH_3)_4Pb$ have been previously noted by Edlund *et al.*[39] and have been attributed to spin−orbit-induced changes in the wave function termed the "heavy-atom shift of the heavy atom" (HAHA effect). All three cases have a lone pair orbital at lead. Relativistic extended Hückel calculations for PbH_3^- and SnH_3^- reveal very large paramagnetic contributions to the shielding of the heavy atom. A similar spin−orbit effect is likely operative for the tin, lead, thallium, and chalcogen chemical shifts of $M_2Ch_3^{2-}$, $TlMTe_3^{3-}$ and related heavy main-group anions (for example, see refs 27 and 32).

Electronegativity differences generally fail to account for the observed shielding trends among $M_2Ch_3^{2-}$ and $TlMTe_3^{3-}$ anions. This is exemplified by the substitution of a Tl atom for a Pb atom in $Pb_2Te_3^{2-}$, which results in increased shielding of the tellurium resonance but significant deshielding of the lead resonance of $TlPbTe_3^{3-}$ relative to that of $Pb_2Te_3^{2-}$ (Table 4). The lower electronegativity of thallium(I) and increased anion charge of $TlPbTe_3^{3-}$ are expected to result in increased shielding of both the tellurium and lead resonances upon substitution of the less electronegative thallium atom for a lead atom. The thallium resonance of $TlSnTe_3^{3-}$ was found to be significantly deshielded relative to that of $TlPbTe_3^{3-}$ and is again the opposite trend expected on the basis of the Sn(II)−Pb(II) electronegativity difference. In contrast, substitution of a tin atom in the $Sn_2Se_3^{2-}$ anion by a lead atom resulted in the anticipated deshielding of the tin nucleus in the $SnPbSe_3^{2-}$ anion, but lead is deshielded relative to $Pb_2Se_3^{2-}$ and is the opposite trend based on electronegativity arguments. The overall shielding trends for the chalcogens in the series $Pb_2Se_3^{2-} \rightarrow SnPbSe_3^{2-} \rightarrow Sn_2Se_3^{2-}$ and $TlPbTe_3^{3-} \rightarrow TlSnTe_3^{3-}$ are also opposite to those anticipated on the basis of the Pb−Sn electronegativity difference. A similar trend is noted for the series $Pb_2Se_xTe_{3-x}^{2-}$ [4] in which the ^{207}Pb chemical shift exhibits a chalcogen dependence analogous to the normal halogen dependence exhibited by the ^{207}Pb and ^{119}Sn resonances of the Pb(II) and Sn(II) halides in

(38) Orbital symmetries under the C_{3v} point symmetry of $TlPbTe_3^{3-}$ are correlated to D_{3h} as follows ($D_{3h} \rightarrow C_{3v}$): $A_1' \rightarrow A_1$, $A_2'' \rightarrow A_1$, $E' \rightarrow E$, $E'' \rightarrow E$.

(39) Edlund, U.; Lejon, T.; Pyykkö, P.; Venkatachalam, T. K.; Buncel, E. *J. Am. Chem. Soc.* **1987**, *109*, 5982.
(40) Wrackmeyer, B. *J. Magn. Reson.* **1985**, *61*, 536.

Table 10. Natural Bond Order Analysis[a] in the $M_2Ch_3^{2-}$, $TlMTe_3^{3-}$ (M = Sn, Pb; Ch = S, Se, Te), and $SnPbSe_3^{2-}$ Anions

orbital	orb pop	atom %	% s	% p	s (coeff)	p_x (coeff)	p_y (coeff)	p_z (coeff)
				$Sn_2S_3^{2-}$, ECP/DZP/LDFT[b]				
σ(Sn−S)	1.97	Sn [21.4%]	6.2	93.6	−0.25		−0.81, −0.07	0.52
		S [78.6%]	13.7	86.1	−0.37		0.60	−0.71
σ(Sn−S)*	0.09							
Sn lp	2.00		81.5	18.5	0.90			0.43
S lp	1.98		72.5	27.5	0.85		0.52	
S lp	1.86			100		1.00		
				$Sn_2Se_3^{2-}$, ECP/ECP/LDFT[b]				
σ(Sn−Se)	1.97	Sn [22.6%]	5.8	93.2	−0.24		−0.81, −0.07	0.52
		Se [77.4%]	10.1	89.7	−0.32		0.63	−0.71
σ(Sn−Se)*	0.08							
Sn lp	2.00		82.8	17.2	0.91			0.41
Se lp	1.98		79.8	20.2	0.89		0.45	
Se lp	1.90			100		1.00		
				$Sn_2Te_3^{2-}$, ECP/ECP/LDFT[b]				
σ(Sn−Te)	1.95	Sn [22.6%]	4.8	94.8	−0.22		−0.81	0.53
		Te [77.4%]	8.2	91.6	−0.29		0.64	−0.71
σ(Sn−Te)*	0.10							
Sn lp	1.99		85.7	14.3	0.91			0.38
Te lp	1.98		83.5	16.5	0.91		0.41	
Te lp	1.90			100		1.00		
				$Pb_2S_3^{2-}$, ECP/DZP/LDFT[b]				
σ(Pb−S)	1.97	Pb [21.9%]	4.6	95.3	−0.20, 0.09		−0.81, 0.08	0.54
		S [78.1%]	10.8	89.1	−0.33		0.63	−0.71
σ(Pb−S)*	0.09							
Pb lp	2.00		88.2	11.8	0.94			0.34
S lp	1.98		78.4	21.6	0.89		0.46	
S lp	1.86			100		1.00		
				$Pb_2Se_3^{2-}$, ECP/ECP/LDFT[b]				
σ(Pb−Se)	1.97	Pb [22.4%]	4.6	95.2	−0.19, 0.11		−0.81	0.54
		Se [77.6%]	8.0	91.8	−0.28		0.65	−0.71
σ(Pb−Se)*	0.08							
Pb lp	2.00		89.3	10.7	0.94			0.33
Se lp	1.99		84.0	16.0	0.92		0.40	
Se lp	1.90			100		1.00		
				$Pb_2Te_3^{2-}$, ECP/ECP/LDFT[b]				
σ(Pb−Te)	1.95	Pb [24.8%]	3.9	95.9	−0.17, 0.10		−0.81	0.54
		Te [75.2%]	7.4	92.4	−0.27		0.65	−0.71
σ(Pb−Te)*	0.11							
Pb lp	1.99		91.2	8.8	0.96			0.29
Te lp	1.98		85.2	14.8	0.92		0.39	
Te lp	1.90			100		1.00		
				$SnPbSe_3^{2-}$, ECP/ECP/ECP/LDFT[c]				
σ(Sn−Se)	1.97	Sn [22.5%]	5.6	94.0	−0.23		−0.81	−0.52
		Se [77.5%]	10.3	89.6	−0.32		0.64	0.70
σ(Pb−Se)	1.97	Pb [22.6%]	4.8	95.0	0.20, −0.11		0.81	−0.53
		Se [77.4%]	7.9	91.9	0.28		−0.64	0.71
σ(Sn−Se)*	0.08							
σ(Pb−Se)*	0.08							
Sn lp	2.00		83.4	16.6	0.91			−0.40
Pb lp	2.00		89.0	11.0	0.94			0.33
Se lp	1.99		81.8	18.2	0.90		0.43	
Se lp	1.90			100		1.00		
				$TlPbTe_3^{3-}$, ECP/ECP/ECP/LDFT[d]				
σ(Tl−Te)	1.91	Tl [14.9%]	3.1	96.5	−0.14, 0.10		−0.81	−0.55
		Te [85.1%]	6.1	93.9	−0.25		0.60	0.76
σ(Pb−Te)	1.95	Pb [23.3%]	5.3	94.6	0.17, −0.16		0.82	−0.53
		Te [76.7%]	10.0	90.0	0.31		−0.69	0.65
σ(Tl−Te)*	0.08							
σ(Pb−Te)*	0.16							
Tl lp	2.00		94.0	6.0	0.97			−0.24
Pb lp	2.00		90.7	9.3	0.95			0.30
Te lp	1.98		84.0	16.0	0.92		0.40	
Te lp	1.91			100		1.00		
				$TlSnTe_3^{3-}$, ECP/ECP/ECP/LDFT[e]				
σ(Tl−Te)	1.92	Tl [14.9%]	2.8	96.9	−0.14, 0.09		−0.81	−0.55
		Te [85.1%]	7.0	92.9	−0.27		0.59	0.76
σ(Sn−Te)	1.96	Sn [25.2%]	5.3	94.5	0.21, −0.09		0.81	−0.53
		Te [74.8%]	10.2	89.7	0.32		−0.69	0.65
σ(Tl−Te)*								
σ(Sn−Te)*								
Tl lp	2.00		93.9	6.1	0.97			−0.24
Sn lp	2.00		86.3	13.7	0.93			0.37
Te lp	1.98		82.8	17.2	0.91		0.41	
Te lp	1.91			100		1.00		

[a] The symbol lp denotes an electron lone pair. [b] Where M−M was chosen as the *z*-axis, the three Ch were in the *x*,*y* plane, with one Ch along the *y*-axis. For the D_{3h} structures, the metal is at +*z*. [c] Sn is at −*z* and Pb at +*z*. [d] Tl is at −*z* and Pb is at +*z*. [e] Tl is at −*z* and Sn is at +*z*.

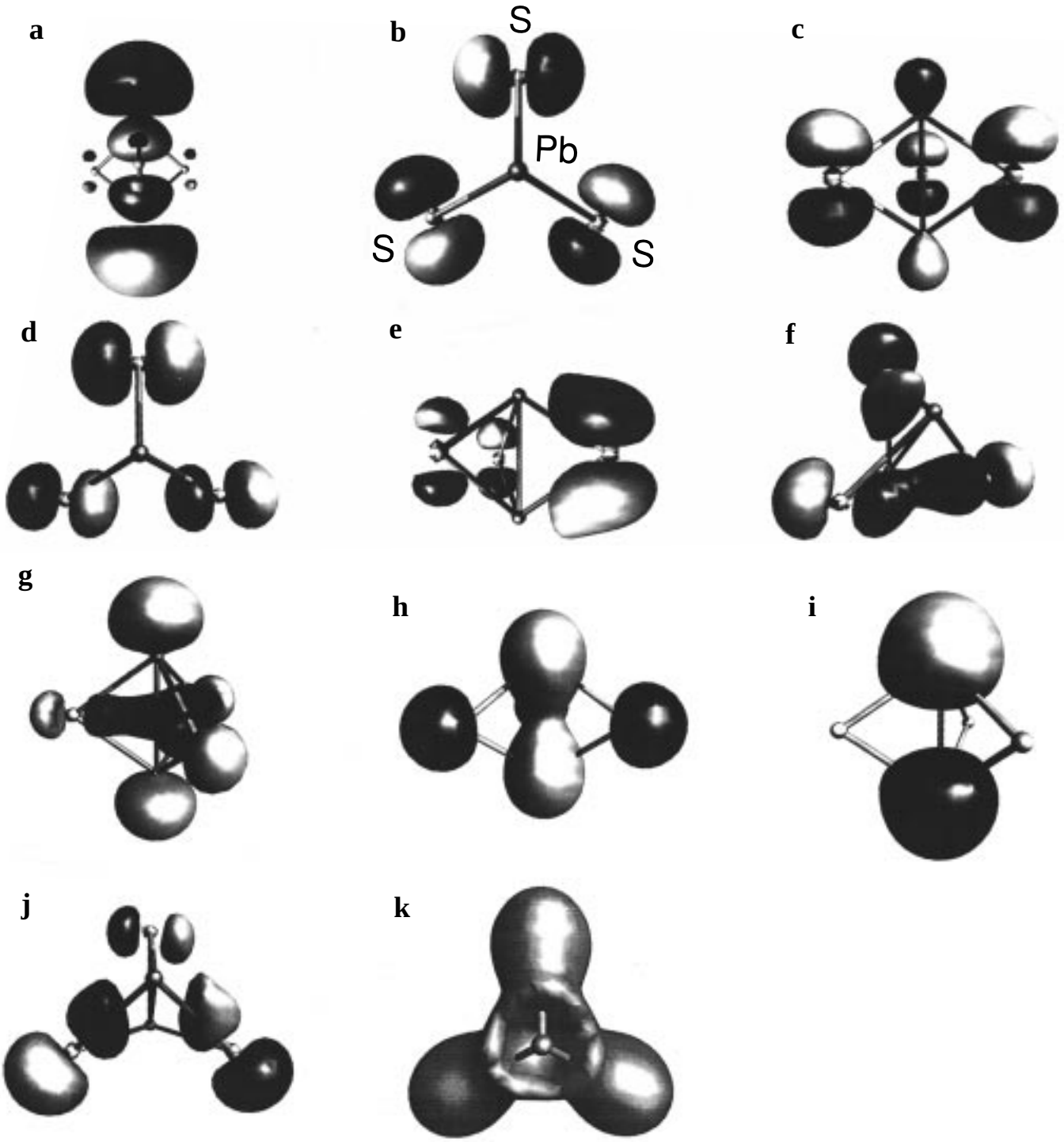

Figure 6. Wave function plots of the LUMO and valence molecular orbitals for the $Pb_2S_3^{2-}$ anion at the LDFT level and contoured at 0.04. The atom labeling scheme is given in (b) and the different shades denote the two different phases of the orbitals. Key: (a) LUMO (A_2''); (b) HOMO (A_2'); (c) NHOMO (A_1''); (d) third and fourth (E′); (e) fifth and sixth (E″); (f) seventh and eighth (E′); (g) ninth (A_1'); (h) tenth (A_1'); (i) eleventh (A_2''); (j) twelfth and thirteenth (E′); and (k) fourteenth (A_1') orbitals.

the solid state,[41] i.e., increased shielding of the group 14 element when descending the halogen or chalcogen group. These trends are also observed for the thallium and chalcogen shieldings over the series of trigonal planar $TlSe_{3-x}Te_x^{3-}$ anions. It has recently been shown that the "heavy-atom shift" on a neighboring atom through spin−orbit-induced changes in the wave function is strongly shielding, increasing with the atomic number and hyperfine integral of the heavy atom neighbor.[42] Spin−orbit effects appear to be related to the presence of free valence electron pairs on the chalcogens and group 13 and 14 elements with their magnitudes depending on the extent to which the valence s orbital is used for bonding to the heavy atom substituent. While the σ bonds of the $M_2Ch_3^{2-}$ and $TlMTe_3^{3-}$ anions are largely p in character, their s characters have been shown to be significant at ca. 6−9% (see "Computational Results"). With the exception of tin in $Sn_2Se_3^{2-}$ and $SnPbSe_3^{2-}$, all of the group 13/14 and chalcogen chemical shift changes

(41) Duchateau, M. Dissertation, Universität Dortmund, 1994.

(42) Kaupp, M.; Malkina, O. L.; Malkin, V. G.; Pyykkö, P. *Chem. Eur. J.* **1998**, *4*, 118.

that result from substitution of a lighter atom(s) by a heavier atom(s) in the present and previously reported series of trigonal bipyramidal anions,[4,5] as well as the $TlSe_{3-x}Te_x^{3-}$ [32] anions, result in increased shieldings.

(d) Coupling Constants. The spin−spin couplings between the axial metal atoms in $TlMTe_3^{3-}$ are the first (Pb) and second (Sn) examples of Tl(I)−M(II) couplings to be reported. The Tl(I)−M(II) couplings in structurally related $MTlO_3(t\text{-Bu})_3$ are 1293 Hz (Sn)[16] and 710 Hz (Pb)[43] are significantly smaller than in $TlMTe_3^{2-}$. In addition, $J(^{119}Sn-^{203,205}Tl)$ values of 519−800 Hz have been reported for the fluxional $Sn_{8-x}Pb_xTl^{5-}$ (x = 0−4) cluster anions,[44−48] but no Tl−Pb couplings were observed.

Pyykkö and Wiesenfeld[49] have shown that relativistic effects on the s electron density of the dominant Fermi contact term[50,51] in the indirect spin−spin coupling (J_{AB}) between nuclei of heavy main-group atoms A and B contribute significantly to the reduced coupling constant, K_{AB}. Previous work on heavy element spin−spin couplings in classically bonded main-group anions[32,18] has illustrated a method for factoring out the relativistic effects on the valence s electron density term, $|\psi_{ns}(0)|^2$, in the Fermi contact contribution to give the relativistically corrected reduced coupling constant, $(K_{AB})_{RC}$. The relative magnitudes of the reduced and relativistically corrected reduced coupling constants corresponding to the M−Ch, Tl−Ch, M−M, and Tl−M (M = Sn, Pb; Ch = Se, Te) nuclear spin−spin couplings are compared in Table 4.

The $(K_{M-Ch})_{RC}$ and $(K_{Tl-Te})_{RC}$ values of $M_2Ch_3^{2-}$, $SnPbSe_3^{2-}$, and $TlMTe_3^{3-}$ anions are significantly smaller than $(K_{Sn-Ch})_{RC}$ values ($\times 10^{20}$ T^2 J^{-1}) reported for anions in which the Sn−Ch bonds have higher formal s characters, i.e., the sp^2-hybridized $SnCh_3^{2-}$ (Se, 144.5; Te, 149.1) and sp^3-hybridized $SnCh_4^{4-}$ (Se, 103.1; Te, 100.6) anions;[39] the tetrahedral $Sn(SPh)_x(SePh)_y(TePh)_{4-x-y}$ molecule where $x = 0-3$ and $y = 0-4$ (Se, 97.0−123.3; Te, 115.0−162.6)[52] and the trigonal pyramidal $Sn(SePh)_3^-$ [51.8],[25] $Sn_2Ch_6^{4-}$ (Se: monoselenide bridge (Se_{mb}) 62.6, terminal (Se_t) 141.3; Te_{mb} 57.3, Te_t 136.4)[18] and $Sn_2Ch_7^{4-}$ (Se: diselenide bridge (Se_{db}) 80.0, Se_{mb} 93.3, Se_t 143.5; Te_{db} 80.0, Te_{mb} 98.8, Te_t 138.7),[18] and adamantanoid $Sn_4Se_{10}^{4-}$ (Se_{mb} 107.9, Se_t 160.4)[53] anions. Large one-bond $(K_{Tl-Ch})_{RC}$ values have also been reported for the formally sp^2-hybridized trigonal planar $TlCh_3^{3-}$ anion [Se, 152.5; Te, 163.6],[32] and contrast with the significantly smaller values reported for the butterfly-shaped $Tl_2Ch_2^{2-}$ [Se, 47.48; Te, 40.52] anions.[27,32] The magnitudes of the $Tl_2Ch_2^{2-}$ coupling constants are consistent with theory which indicates that the Tl−Ch σ bonds have high p character (calculated % s characters: Se, 10.4%; Te, 8.7%).[27] Two previous studies have suggested that the M−Ch σ-bonding of the $M_2Ch_3^{2-}$ anions is essentially pure p in character.[4,5] The NBO analyses of members of the trigonal bipyramidal anion series reported in the present study are basically consistent with this view but show that these bonds also have low but significant s characters which range from ca. 6−10% (see "Computational Results" and Table 10). The magnitudes of the $(K_{M-Ch})_{RC}$ and $(K_{Tl-Te})_{RC}$ values of the trigonal bipyramidal anions are, however, significantly smaller than those of the $Tl_2Ch_2^{2-}$ anions[27] where % s characters are not significantly different (Table 4). No obvious pattern emerges which links the Fermi contact dominated relativistically corrected reduced spin−spin couplings of the trigonal bipyramidal anions to the % s characters of their M−Ch or Tl−Te bonds. In the more limited anion series $Sn_2Se_3^{2-}$, $SnPbSe_3^{2-}$, $Pb_2Se_3^{2-}$, the % s characters for the M−Se bonds and their M−Se couplings are correlated. The bonding is very similar over series and is reflected in the similarities of their NBO analyses and natural orbital populations. In contrast, the % s characters of the Sn−Te and Pb−Te bonds in the $TlSnTe_3^{3-}$ and $TlPbTe_3^{3-}$ anions are very similar but $TlSnTe_3^{3-}$ exhibits a $(K_{Sn-Te})_{RC}$ value which is approximately five times larger than its lead analogue. Similarly, the $(K_{Sn-Se})_{RC}$ values are approximately three times larger than the $(K_{Pb-Se})_{RC}$ values in the $Sn_2Se_3^{2-}$, $SnPbSe_3^{2-}$, $Pb_2Se_3^{2-}$ series.

The relative magnitudes of $(K_{M-M})_{RC} > (K_{M-Ch})_{RC}$ in the trigonal bipyramidal anions are generally consistent with the calculated relative s characters of their M−M (Mayer bond orders, 0.13−0.32; 100% s character) and M−Ch (Mayer bond orders, 0.72−0.96; 5.6−9.0%) bonds. This contrasts with the $(K_{Tl-Ch})_{RC}$ values of the $Tl_2Ch_2^{2-}$ (Ch = Se and/or Te) anions which are approximately 2−5 times larger than their $(K_{Tl-Tl})_{RC}$ values and opposite to their relative Mayer bond orders and % s characters; Tl−Tl (0.14−0.15; 100% s character) and Tl−Ch (Se, 0.79−0.95; 8.7% s character; Te, 0.82−0.99, 10.4% s character).[27] Overall, the M−M and Tl−M bond orders with their assumed 100% s characters are similar to or greater than in the $Tl_2Ch_2^{2-}$ anions and apparently do not fully account for the abnormally large values for the $(K_{M-M})_{RC}$ couplings relative to those of the $Tl_2Ch_2^{2-}$ anions. The differences may arise from the additivity of the multiple coupling pathways through the M−Ch framework as well as from transannular through-space interactions between the bridgehead M atoms. The M−M and Tl−M couplings in $M_2Ch_3^{2-}$ and $TlMTe_3^{3-}$ can be transmitted through the three available M−Ch−M (M−Te−Tl) coupling pathways whereas only two coupling pathways are available in $Tl_2Ch_2^{2-}$. The M−Ch−M bond angles are considerably larger in $Tl_2Ch_2^{2-}$ (∼90°) than in the trigonal bipyramidal anions (∼55−70°) and may also influence the relative magnitudes of $K(M-M)_{RC}$ observed in the two anion series.[54]

Conclusion

The solution structures of the $TlMTe_3^{3-}$ anions have been studied by multi-NMR spectroscopy and confirmed by an analysis of the first-order ^{119}Sn, ^{125}Te, ^{205}Tl, and ^{207}Pb subspectra arising from natural abundance isotopomer distributions. The X-ray crystal structures of the $Pb_2S_3^{2-}$ and $TlSnTe_3^{3-}$ anions have been determined for the first time and that of $Pb_2Se_3^{2-}$ has been redetermined at low temperature to reveal that the elongated ellipsoids previously noted in the crystal structures of this anion and those of $Pb_2S_3^{2-}$, $Pb_2Te_3^{2-}$, $Sn_2Se_3^{2-}$, and $Sn_2Te_3^{2-}$ do not arise from a disorder but from a rocking motion of the anion. Density functional theory calculations confirmed

(43) Veith, M.; Mathur, S., private communication.
(44) Rudolph, R. W.; Wilson, W. L.; Parker, F.; Taylor, R. C.; Young, D. C. *J. Am. Chem. Soc.* **1978**, *100*, 4629.
(45) Rudolph, R. W.; Taylor, R. C.; Young, D. C. In *Fundamental Research in Homogeneous Catalysis*; Tsutsui, M., Ed.; Plenum Press: New York, 1979; p 997.
(46) Pons, B. S.; Santure, D. J.; Taylor, R. C.; Rudolph, R. W. *Electrochem. Acta* **1981**, *26*, 365.
(47) Rudolph, R. W.; Wilson, W. L. *J. Am. Chem. Soc.* **1981**, *103*, 2480.
(48) Wilson, W. L.; Rudolph, R. W.; Lohr, L. L.; Taylor, R. C.; Pyykkö, P. *Inorg. Chem.* **1986**, *25*, 1535.
(49) Pyykkö, P.; Wiesenfeld, L. *Mol. Phys.* **1981**, *43*, 557.
(50) Jameson, C. J. In *Multinuclear NMR*; Mason, J., Ed.; Plenum Press: New York, 1987; Chapter 4, p 89.
(51) Pople, J. A.; Santry, D. P. *Mol. Phys.* **1964**, *8*, 1.
(52) Dean, P. A. W.; Srivastava, R. S. *Inorg. Chim. Acta* **1985**, *105*, 1.
(53) Campbell, J.; DiCiommo, D. P.; Mercier, H. P. A.; Pirani, A. M.; Schrobilgen, G. J. *Inorg. Chem.* **1995**, *34*, 6265.
(54) Mason, J. In *Multinuclear NMR*; Mason, J., Ed.; Plenum Press: New York, 1987; Chapter 4, pp 108, 109.

that the trigonal bipyramidal geometries are true minima. The calculated frequencies are in good agreement with the experimental Raman frequencies. Theory indicates that the M−Ch bonds are two-center two-electron bonds of high p character and that there is a significant concentration of s electron density between the M atoms corresponding to Mayer bond orders of 0.13−0.32. The extreme high frequency shifts of lead and thallium apparently result from spin−orbit induced changes in the wave function, or the so-called "heavy-atom shift of the heavy atom" (HAHA effect). Likewise, the large deshieldings observed for group 13/14 metal and chalcogen NMR resonances upon substitution of a neighboring heavy atom are attributable to spin−orbit-induced heavy-atom substituent effects. The relative magnitudes of the Fermi contact dominated $(K_{M-M})_{RC}$, $(K_{M-Ch})_{RC}$, $(K_{Tl-M})_{RC}$, and $(K_{Tl-Te})_{RC}$ coupling constants are consistent with the theoretical findings. The weak M−M and Tl−M bonding interactions are essentially s in character with correspondingly large couplings as compared to the high p characters of the M−Ch and Tl−Te bonds with their significantly smaller couplings.

Experimental Section

Apparatus and Materials. All compounds employed are air sensitive. Consequently, all manipulations were performed under rigorously anhydrous conditions and in the absence of oxygen on vacuum lines and in a drybox as previously described in ref 27.

Potassium metal (BDH Chemicals, >99%) was cleaned as previously described, and freshly cut samples were handled only in the drybox. Thallium rod (Alfa Inorganics, 99%), lead shot (BDH Chemicals, 99.99%), tin granules (Baker Analyzed Reagent, 99.9%), tellurium powder (Alfa Inorganics, 99.5%), sulfur powder (BDH Chemicals), and 2,2,2-crypt (4,7,13,16,21,24-hexaoxa-1,10-diazabicyclo[8.8.8] hexacosane; Merck, 99%) were dried in the evacuated port of the drybox for a minimum of 45 min followed by exposure to the drybox atmosphere for at least 2 days prior to use. The oxide layer on the thallium rod was trimmed off with a scalpel inside the drybox prior to use. Potassium monotelluride, K_2Te, and potassium monosulfide, K_2S, were prepared as previously described in ref 4.

All solvents were thoroughly dried, transferred by vacuum distillation, and stored in 250 mL round-bottom Pyrex flasks equipped with 6-mm glass/Teflon stopcocks (J. Young Scientific). Tetrahydrofuran (Fisher, 99.9%) was stored over freshly cut sodium wire (BDH Chemicals, 99.8%). Ethylenediamine (Aldrich, 99%) and ethylamine (Aldrich, 99%) were dried over CaH_2 powder (BDH Chemicals) for several weeks and then vacuum distilled onto, and stored over, fresh CaH_2 for at least an additional week prior to use. Anhydrous ammonia (Matheson, 99.99%) was condensed from a gas cylinder at −78 °C into a previously dried tube containing freshly cut sodium metal and stored at −78 °C for at least 1 week prior to use.

Alloy Preparation. The ternary $KPb_{0.8}S$, $KPb_{0.5}Se$, and $Tl_2M_2Te_3$ (M = Sn, Pb) alloys were prepared as previously described[4] by fusion of the elements in the required molar ratios inside thick-walled Pyrex tubes. KPbS: K, 0.3412 g, 8.727 mmol; Pb, 1.8066 g, 8.719 mmol; S, 0.2801 g, 8.737 mmol. KPbSe: K, 0.6212 g, 15.89 mmol; Pb, 3.2891 g, 15.874 mmol; Se, 1.2532 g, 15.871 mmol. $Tl_2Pb_2Te_3$: Tl, 2.0030 g, 9.801 mmol; Pb, 2.0294 g, 9.794 mmol; Te, 1.8789 g, 14.725 mmol. $Tl_2Sn_2Te_3$: Tl, 1.0790 g, 5.280 mmol; Sn, 0.6353 g, 5.353 mmol; and Te, 1.0676 g, 8.367 mmol. The resulting alloys were ground into fine powders, and the compositions of the KPbS and KPbSe alloys were corrected for the recovered lead lumps (0.4222 g, 2.038 mmol and 1.6803 g, 8.109 mmol) to $KPb_{0.8}S$ and $KPb_{0.5}Se$.

Preparation of $TlMTe_3^{3-}$ (M = Sn, Pb) Solutions for NMR Spectroscopy. The anions were prepared by the reaction of the $Tl_2M_2Te_3$ alloys with K_2Te in en (Sn) or in 1:1 v/v en/ethylamine mixtures (Pb) in the presence of a stoichiometric excess of 2,2,2-crypt with respect to K^+. The resulting deep red solutions were isolated for NMR spectroscopy as previously described. $TlSnTe_3^{3-}$ ($Tl_2Sn_2Te_3$, 0.1797 g, 0.172 mmol; K_2Te, 0.0522 g, 0.254 mmol; 2,2,2-crypt, 0.1958 g, 0.520 mmol). $TlPbTe_3^{3-}$ ($Tl_2Pb_2Te_3$, 0.0836 g, 0.069 mmol; K_2Te, 0.0219 g, 0.106 mmol; 2,2,2-crypt, 0.2037 g, 0.541 mmol).

Multinuclear Magnetic Resonance Spectroscopy. ^{207}Pb and ^{119}Sn NMR spectra were recorded on Bruker AM-500 (11.744 T) and Bruker AC-300 (7.0463 T) pulse spectrometers, respectively. The ^{125}Te NMR spectra were recorded either on a Bruker AM-500 ($TlPbTe_3^{3-}$) or on a Bruker AC-300 ($TlSnTe_3^{3-}$) pulse spectrometer. Spectra were routinely obtained without locking (field drift < 0.1 Hz h^{-1}) using 10-mm probes broad banded over the frequency ranges 13.968−121.497 (7.0463 T) and 23.276−202.460 MHz (11.744 T). The spectrometer frequencies were 104.631 (^{207}Pb), 111.922 (^{119}Sn), 157.794 MHz (^{125}Te, 11.744 T), and 94.692 MHz (^{125}Te, 7.0463 T). Since the ^{205}Tl nucleus resonates outside the dynamic frequency ranges of the Bruker AC-300 (172.902 MHz) and the AM-500 (288.169 MHz) broad-band probes, ^{205}Tl NMR spectra were recorded on a Bruker AC-200 (4.698 T) pulse spectrometer by inserting the 10-mm Bruker AC-300 broad-banded probe into the cryomagnet of the AC-200. The spectrometer frequency for ^{205}Tl at 4.698 T was 115.444 MHz. Free-induction decays were typically accumulated in 16 or 32 K memories. Spectral width settings of 25−100 kHz were employed, yielding data point resolutions of 3.05−6.10 Hz/data point and acquisition times of 0.328−0.164 s, respectively. Relaxation delays were not applied. Typically, 40 000−200 000 transients were accumulated depending on the concentrations and sensitivities of the nuclides under study. Pulse-width settings corresponding to a bulk magnetization tip angle, θ, of ~90° were 25.0 (^{207}Pb), 12.5 (^{119}Sn), 10.0 (^{125}Te, 11.744 T), 5.0 (^{125}Te, 7.0463 T), and 20.0 μs (^{205}Tl). Line broadening parameters used in the exponential multiplication of the free induction decays were 10−20 Hz for narrow lines and 100 Hz for broad lines. Variable-temperature spectra were recorded using the variable-temperature controllers of the spectrometers, and temperatures (accurate to ±1.0 °C and stable to within ±0.10 °C) were checked by placing a copper−constantan thermocouple in the sample region of the probe. Samples were allowed to equilibrate for at least 5 min while spinning before spectral accumulations were begun.

The respective nuclei were referenced externally to neat samples of $(CH_3)_4M$ (M = Sn, Pb), $(CH_3)_2Te$, and 0.1 M aqueous $TlNO_3$ at 24 °C. The chemical shift convention used was a positive (negative) sign signifies a chemical shift to high (low) frequency of the reference compound.

The ^{119}Sn, ^{125}Te, ^{205}Tl, and ^{207}Pb NMR subspectra of the $TlMTe_3^{3-}$ anions were simulated and summed by using the program DSYMPC.[55] Subspectra were weighted by using the normalized total line intensities listed in Table 5 and summed by using the line spectrum addition subroutine in DSYMPC.

Raman Spectroscopy. Raman spectra of the $Sn_2Se_3^{2-}$, $Sn_2Te_3^{2-}$, $Pb_2S_3^{2-}$, and $Pb_2Se_3^{2-}$ anions were recorded on a Jobin-Yvon Mole S-3000 triple-spectrograph system equipped with a 0.32-m prefilter, adjustable 25-mm entrance slit, and a 1.00-m monochromator. Holographic gratings were used for the prefilter (600 grooves mm^{-1}, blazed at 500 nm) and monochromator (1800 grooves mm^{-1}, blazed at 550 nm) stages. An Olympus metallurgical microscope (model BHSM-L-2) was used for focusing the excitation laser to a 1-μm spot on the sample. The 514.5-nm ($Sn_2Se_3^{2-}$ and $Pb_2S_3^{2-}$) and 647.1-nm ($Sn_2Te_3^{2-}$, $Pb_2Se_3^{2-}$) lines of the Spectra Physics model 2016 Ar^+ ion laser and a Lexel model 2500 Kr^+ ion laser, respectively, were used for sample excitation. Spectra were recorded at ambient temperature on powdered microcrystalline samples of $(2,2,2\text{-crypt-}K^+)_2Sn_2Se_3^{2-}$ and $(2,2,2\text{-crypt-}K^+)_2Pb_2Se_3^{2-}$ and on single crystals of $(2,2,2\text{-crypt-}K^+)_2Sn_2Te_3^{2-}$ and $(2,2,2\text{-crypt-}K^+)_2Pb_2S_3^{2-}\cdot 0.5en$ sealed in Pyrex melting point capillaries that had been previously dried overnight at 200−250 °C under vacuum. The powdered materials were obtained by carefully grinding several crystals inside the drybox using an agate mortar and pestle.

Spectra were recorded by signal averaging using a Spectraview-2D CCD detector equipped with a 25-mm chip (1152 × 298 pixels) and at laser powers of 100−150 mW. A total of 15 reads having 60 s integration times for $(2,2,2\text{-crypt-}K^+)_2Sn_2Te_3^{2-}$ and 90 s integration

(55) Hägele, G.; Höffken, H.-W.; Mistry, F.; Spiske, R.; Weber, U.; Goudetsidis, S. *DSYMPC*, Release 0.940728E.; Institut für Anorganische Chemie und Strukturchemie, Heinrich Heine Universität: Düsseldorf, Germany, 1994.

times for (2,2,2-crypt-K^+)$_2Sn_2Se_3^{2-}$ and (2,2,2-crypt-K^+)$_2Pb_2S_3^{2-}$·0.5en and a total of 30 reads having 180 s integration times for (2,2,2-crypt-K^+)$_2Pb_2Se_3^{2-}$ were summed. Spectral line positions are estimated to be accurate to ±2 cm $^{-1}$. The Raman spectrometer was frequency calibrated by using the 1018.3 cm^{-1} line of neat liquid indene.

The FT-Raman spectra of the $Pb_2Te_3^{2-}$ and $TlPbTe_3^{3-}$ anions were recorded on Bruker RFS 100/S and Equinox 55/FRA 106 spectrometers, respectively. Each system was equipped with an Adlas diode-pumped Nd:YAG laser operating at 1064-nm, an appropriate near-IR beam splitter, a liquid-nitrogen cooled Ge detector, and a Rayleigh notch filter. The spectral range on the Stokes side was 3600 to 70 cm^{-1}. The single crystals were measured in a backscattering geometry in the standard sample compartment. Spectra were acquired at 4 cm^{-1} resolution and a Blackman−Harris function (either 3-term or 4-term) was used to apodize the interferograms. The interferograms were also zerofilled for improved resolution and band shape. For the $TlPbTe_3^{3-}$ anion, a focused laser spot (ca. 0.2 mm) of 60 mW power was used to excite the sample. Five blocks of 500 scans were averaged for a combined acquisition time of 75 min. For the $Pb_2Te_3^{2-}$ anion, a defocused laser spot (ca. 1 mm) of 350 mW was employed. Six blocks of 500 scans were averaged for a total acquisition time of 90 min. A tungsten source was measured and used to correct both spectra for the individual instrument response.

Crystal Structure Determinations of (2,2,2-crypt-K^+)$_3$TlPbTe$_3^{3-}$·2en, (2,2,2-crypt-K^+)Pb$_2$Se$_3^{2-}$·0.5en, and (2,2,2-crypt-K^+)Pb$_2$S$_3^{2-}$·0.5en. Crystal Growing. (2,2,2-crypt-K^+)$_3$TlPbTe$_3^{3-}$·2en. The reaction of the alloys $Tl_2Pb_2Te_3$ (0.0836 g, 0.069 mmol) and K_2Te (0.0219 g, 0.106 mmol) in en in the presence of a molar excess of 2,2,2-crypt (0.2037 g, 0.541 mmol) with respect to K^+ gave rise to a deep red solution which was shown by ^{205}Tl, ^{207}Pb, and ^{125}Te NMR spectroscopy to contain the $TlPbTe_3^{3-}$ anion (90%) and small amounts of $Pb_2Te_3^{2-}$ (10%). As there was no evidence of crystallization in the NMR sample after several weeks, the solution was transferred into one arm of a two-arm Pyrex vessel under the dry nitrogen atmosphere of a glovebag. An excess of THF (1:5 v/v) was vacuum distilled at 0 °C into the second arm of the Pyrex reactor. The reactor was allowed to stand for 5−6 weeks over which the THF slowly vapor-phase diffused into the en solution, resulting in the formation of large, deep-red diamond-shaped crystals. The mother liquor was decanted back into the first arm of the Pyrex vessel and removed under the dry nitrogen atmosphere of a glovebag. The crystalline sample was dried under dynamic vacuum at room temperature and transferred into a drybox for mounting.

(2,2,2-crypt-K^+)Pb$_2$Ch$_3^{2-}$·0.5en (Ch = S, Se). The alloy ($KPb_{0.8}S$, 0.1029 g, 0.4460 mmol; $KPb_{0.5}Se$, 0.0754 g, 0.3402 mmol) was transferred into one arm of a two-arm Pyrex vessel and extracted in en in the presence of a molar excess of 2,2,2-crypt (S, 0.1350 g, 0.359 mmol; Se, 0.1421 g, 0.3774 mmol) with respect to K^+. After 3−4 weeks, the solution (S, yellow-orange; Se, orange) was carefully decanted off the alloy residue into the second arm of the reaction vessel. Yellow [(2,2,2-crypt-K^+)$Pb_2S_3^{2-}$·0.5en] and orange [(2,2,2-crypt-K^+)$Pb_2Se_3^{2-}$·0.5en] rhombohedral crystals were obtained by vapor-phase diffusion of THF into the en extracts.

The crystals used in this study were sealed in Lindemann glass capillaries under dry nitrogen inside a drybox equipped with a stereomicroscope and had the following dimensions: 0.42 × 0.18 × 0.29 mm^3 [(2,2,2-crypt-K^+)$_3$TlPbTe$_3^{3-}$·2en], 0.52 × 0.31 × 0.23 mm^3 [(2,2,2-crypt-K^+)$_2Pb_2S_3^{2-}$·0.5en], and 0.66 × 0.40 × 0.37 mm^3 [(2,2,2-crypt-K^+)$_2Pb_2Se_3^{2-}$·0.5en].

Collection and Reduction of X-ray Data. (2,2,2-crypt-K^+)$_3$TlPbTe$_3^{3-}$·2en. A suitable crystal was centered on a Syntex P3 diffractometer, using silver radiation monochromatized with a graphite crystal (λ = 0.560 86 Å). Accurate cell dimensions were determined at 24 °C from a least-squares refinement of the setting angles (χ, ϕ, and 2θ) obtained from 24 accurately centered reflections (with 15.10 ≤ 2θ ≤ 23.50°) chosen from a variety of points in reciprocal space. Integrated diffraction intensities were collected using an ω scan technique with scan rates varying from 1.5 to 14.6° min^{-1} and a scan range of ±0.5° so that the weaker reflections were examined more slowly to minimize counting errors. The data were collected with 0 ≤ h ≤ 16, 0 ≤ k ≤ 28, and −22 ≤ l ≤ 18 and with 3 ≤ 2θ ≤ 35°. During data collection, the intensities of three standard reflections were monitored every 97 reflections to check for crystal stability and alignment. No crystal decay was observed. A total of 5434 unique reflections remained after averaging of equivalent reflections, and 2272 reflections, satisfying the condition $I > 2\sigma(I)$, were used for structure solution. Corrections were made for Lorentz and polarization effects, and absorption corrections were applied using the program DIFABS.[56]

(2,2,2-crypt-K^+)$_2$M$_2$Ch$_3^{2-}$·0.5THF (Ch = S, Se). The diffraction data of the title compounds were collected at the Max Planck Institut für Festkörperforschung (Stuttgart, Germany) on a Stoe Imaging Plate Diffractometer System. Values for the $Pb_2Se_3^{2-}$ structure, when differing from those of $Pb_2S_3^{2-}$, are given in square brackets. Data were collected in two stages: (a) 500 [667] exposures (4 [3] min per exposure) were obtained at 50 [60] mm with 90 [0]° ≤ φ ≤ 290 [200.1]° and with the crystal oscillated through 0.4 [0.3]° in φ; (b) 222 [200] exposures (4.5 [1.5] min per exposure) were obtained at 125 [120] mm with 90 [0]° ≤ φ ≤ 289.8 [200]° and with the crystal oscillated through 0.9 [1.0]° in φ. The two data sets were merged and the final data set contained 91 [92]% of the calculated number of unique reflections. Computations were carried out on a Silicon Graphics model 4600 PC work station. During refinement, some reflections were either omitted if $F^2 < 0$ or flagged for potential systematic errors. Hydrogen-atom positions were calculated and C−H was fixed to 0.96 Å, with $U_{iso}(H) = -1.2U_{eq}$ of the parent atom. Corrections were made for Lorentz and polarization effects and absorption corrections were applied using an empirical absorption correction based on redundant reflections.

Solution and Refinement of the Structures. All calculations were performed on a Silicon Graphics model 4600PC workstation using the SHELXTL-*Plus* package (Sheldrick, 1994) for structure determination, refinement, and molecular graphics.[57]

The XPREP program[57] was used to confirm the unit cell dimensions and the crystal lattices. A first solution was usually obtained without absorption corrections by using conventional direct methods which located the general and/or special positions of the main group and alkali metal atoms. The full-matrix least-squares refinement of the positions and isotropic thermal parameters of the assigned atoms located the general and/or special positions of the C, N, and O atoms of the 2,2,2-crypt-K^+ cations. Any disorder in the cations was modeled at this point in the refinement. Ethylenediamine solvent molecules were assigned after the atoms of the anions and cations were refined with anisotropic thermal parameters and any disorder was satisfactorily modeled. Crystallographically well-behaved solvent molecules were refined with anisotropic thermal parameters, whereas disordered solvent molecules were isotropically refined at 0.5 occupancy by constraining the C−C, C−N, and C−O bond lengths and the nonadjacent C−N and C−O distances to values observed in ordered solvent molecules. Hydrogen atom positions were usually calculated (d(C−H) = 0.96 Å, d(O−H) = 0 0.82 Å, d(N−H) = 0.96 Å), and U(H) was fixed to −1.2 × U(C), U(O), or U(N). The final solutions were obtained by using data that had been corrected for absorption. During the final stages of the refinement, all reflections with $F^2 < -2\sigma(F^2)$ were suppressed and weighting factors recommended by the refinement program were introduced. The maximum electron densities, in the final difference Fourier maps, were located around the anions.

The location of the apical atoms (Tl/Pb) of the $TlPbTe_3^{3-}$ anion on one general position implied a 50:50 positional disorder and indicated that the apical atoms were equivalent by symmetry. The apical atom position was therefore refined as 0.5 Tl and 0.5 Pb.

Computational Methods. Density functional theory calculations were done with the program DGauss[58] at the local (LDFT) and nonlocal (NLDFT) (gradient-corrected) levels. Calculations for the Sn clusters were done with an all-electron polarized double-ζ valence basis set

(56) Walker, N.; Stuart, D. *Acta Crystallogr.* **1983**, *A39*, 158.
(57) Sheldrick, G. M. *SHELXTL-Plus*, Release 4.21/V; Siemens Analytical X-ray Instruments Inc.: Madison, WI, 1993.
(58) (a) Andzelm, J.; Wimmer, E.; Salahub, D. R. In *The Challenge of d and f Electrons: Theory and Computation*; Salahub, D. R., Zerner, M. C., Eds.; ACS Symposium Series 394; American Chemical Society: Washington DC, 1989; p 228. (b) Andzelm, J. In *Density Functional Theory in Chemistry*; Labanowski, J., Andzelm, J., Eds.; Springer-Verlag: New York, 1991; p. 155. (c) Andzelm, J.; Wimmer, E. *J. Chem. Phys.* **1992**, *96*, 1280.

(DZVP).[59] Calculations on the Pb clusters were done with a basis set in which the Pb core electrons are treated with a pseudopotential (PP), and the remaining electrons are treated with a polarized valence double-ζ basis set.[60] For the chalcogens, calculations were done with a polarized double-ζ valence basis set[59] (DZVP2 for S and DZVP for Se and Te) as well as with pseudopotentials on the chalcogens. The local potential fit of Vosko, Wilk, and Nusair[61] (VWN) was used. The gradient-corrected or nonlocal density functional calculations were done with the nonlocal exchange potential of Becke[62] together with the nonlocal correlation function of Perdew[63] (BP/PP/PP and BP/PP/DZVP). The geometries were optimized by using analytic gradient methods. Second derivatives were calculated by numerical differentiation of the analytic first derivatives for the calculations with pseudopotentials whereas analytic methods were used for the all-electron calculations.[64] For the finite difference calculations, a two-point method with a finite difference of 0.01 au was used. Bond orders and valencies were calculated following the method of Mayer.[37] In the case of $TlSnTe_3^{3-}$, Mayer valencies and Mayer bond orders could not be calculated because of a lack of convergence.

Separate calculations at the local level were done with the program Gaussian94[65] in order to test the sensitivity of the results to the form of the treatment of the core electrons. For the calculations on the Sn anions, we used the effective core potentials (ECP) and basis sets of Hay and Wadt[66] augmented by d polarization functions taken from Huzinaga's compilation for Sn, Se, and Te and an all-electron polarized double-ζ basis set for S.[67] For the Pb calculations, we used the ECP of Stevens and co-workers[68] for Pb and the remaining atoms were treated as described above. The ECP results were obtained by using the natural bond orbital (NBO) method of Weinhold and co-workers.[69] All orbital plots were obtained with the UniChem program.

Acknowledgment. We thank the Natural Sciences and Engineering Research Council (NSERC) of Canada for support in the form of a research grant. We also thank NSERC Canada and Ontario Ministry of Education and Training for the award of graduate scholarships to J.C. and A.M.P., respectively. We gratefully acknowledge Prof. Dr. Arndt Simon, Max Planck Institut für Festkörperforschung (Stuttgart, Germany) for making the Stoe imaging plate diffractometer system available and Janice Hellman (Bruker Spectrospin, Milton, Ontario, Canada) and Nancy Kawai (Bruker Optics, Billerica, MA) for recording the Raman spectra of $Pb_2Te_3^{2-}$ and $TlPbTe_3^{3-}$. The density functional theory calculations were performed under the auspices of the Office of Basic Energy Sciences, U.S. Department of Energy, under Contract DE-AC06-76RLO 1830 with the Battelle Memorial Institute, which operates the Pacific Northwest National Laboratory, a multiprogram national laboratory operated from the Department of Energy.

Supporting Information Available: Crystal data and structure refinement parameters (Table S1), atomic coordinates and equivalent isotropic displacement parameters for the 2,2,2-crypt-K^+ cations (Tables S2, S6, and S10), bond lengths and bond angles in the 2,2,2-crypt-K^+ cations (Tables S3, S7, and S11), anisotropic displacement parameters (Tables S4, S8, and S12), atomic coordinates for the hydrogen atoms (Tables S5, S9, and S13), and correlation diagrams for the vibrational modes of the $M_2Ch_3^{2-}$ (M = Sn, Pb; Ch = Se, Te), $Pb_2S_3^{2-}$, and $TlPbTe_3^{3-}$ anions (S14) (25 pages). Ordering information is given on any current masthead page.

IC980574T

(59) Godbout, N.; Salahub, D. R.; Andzelm, J.; Wimmer, E. *Can. J. Chem.* **1992**, *70*, 560.
(60) Chen, H.; Kraskowski, M.; Fitzgerald, G. *J. Chem. Phys.* **1993**, *98*, 8710. (b) Troullier, N.; Martins, J. L. *Phys. Rev. B*, **1991**, *43*, 1993.
(61) Vosko, S. J.; Wilk, L.; Nusair, W. *Can. J. Phys.* **1980**, *58*, 1200.
(62) (a) Becke, A. D. *Phys. Rev. A* **1988**, *38*, 3098. (b) Becke, A. D. In *The Challenge of d and f Electrons: Theory and Computation*; Salahub, D. R.; Zerner, M. C., Eds.; ACS Symposium Series 394; American Chemical Society: Washington DC, 1989; p 166. (c) Becke, A. D. *Int. J. Quantum. Chem. Symp.* **1989**, *23*, 599.
(63) Perdew, J. P. *Phys. Rev. B* **1986**, *33*, 8822.
(64) Komornicki, A.; Fitzgerald, G. *J. Phys. Chem.* **1993**, *98*, 1398 and references therein.
(65) Frisch, M. J.; Trucks, G. W.; Schlegel, H. B.; Gill, P. M. W.; Johnson, B. G.; Robb, M. A.; Cheeseman, J. R.; Keith, T. A.; Peterson, G. A.; Montgomery, J. A.; Raghavachari, K.; Al-Laham, M. A.; Zakrzewski, V. G.; Ortiz, J. V.; Foresman, J. B.; Cioslowski, J.; Stefanov, B. B.; Nanayakkara, A.; Challacombe, M.; Peng, C. Y.; Ayala, P. Y.; Chen, W.; Wong, M. W.; Andres, J. L.; Replogle, E. S.; Gomperts, R.; Martin, R. L.; Fox, D. J.; Binkley, J. S.; Defrees, D. J.; Baker, J.; Stewart, J. J. P.; Head-Gordon, M.; Gonzalez, C.; Pople, J. A. *Gaussian 94*; Gaussian, Inc.: Pittsburgh, PA, 1995.
(66) Hay, P. J.; Wadt, W. R. *J. Chem. Phys.* **1985**, *82*, 270, 284, 299.
(67) Huzinaga, S.; Andzelm, J.; Klobukowski, M.; Radzio-Andzelm, E.; Sakai, Y.; Tatewaki, H. *Gaussian Basis Sets for Molecular Calculations*; Physical Sciences Data Series 16; Elsevier: Amsterdam, 1984.
(68) Stevens, W. J.; Krauss, M.; Basch, H.; Jasien, P. G. *Can. J. Chem.* **1992**, *70*, 216.
(69) (a) Reed, A. E.; Curtiss, L. A.; Weinhold, F. *Chem. Rev.* **1988**, *88*, 899. (b) Foster, J. P.; Weinhold, F. J. *J. Am. Chem. Soc.* **1980**, *102*, 7211. (c) Reed, A. E.; Weinhold, F. *J. Chem. Phys.* **1983**, *78*, 4066. (d) Reed, A. E.; Weinstock, R. B.; Weinhold, F. *J. Chem. Phys.* **1985**, *83*, 735. (e) Reed, A. E.; Weinhold, F. *J. Chem. Phys.* **1985**, *83*, 1736.